Strength and Stress Evolution of an Actively Exhuming Low-Angle Normal Fault, Woodlark Rift, SE Papua New Guinea

Marcel Mizera[1], Tim Little[1], Carolyn Boulton[1], Yaron Katzir[2], Nivedita Thiagarajan[3], David J. Prior[4], James Biemiller[5], Euan G.C. Smith[1]

[1]School of Geography, Environment and Earth Sciences, Victoria University of Wellington, Wellington, New Zealand.

[2]Department of Geological and Environmental Sciences, Ben Gurion University of the Negev, Israel.

[3]Division of Geological and Planetary Sciences, California Institute of Technology, Pasadena, CA 91125

[4]Department of Geology, University of Otago, Dunedin, New Zealand.

[5]Institute for Geophysics, Jackson School of Geosciences, University of Texas at Austin, Austin, Texas, USA.

Corresponding author: Marcel Mizera (marcel.mizera@vuw.ac.nz)

Key Points:

- The active Mai'iu low-angle normal fault dips ~20° at the surface, but is steeper at depth.
- A differential stress peak of 140–185 MPa at 6–12 km depth was identified in a zone of mixed-mode seismic- and aseismic slip.
- High differential stresses drive slip on a ~35° dipping part of this fault and cause new brittle yielding of strong mafic footwall rocks.
- The Mai'iu fault is frictionally weak near the surface ($\mu \approx 0.15–0.38$), but strong in the middle crust ($\mu > 0.25–0.62$).
- Reconstructed principal stresses are constrictional and consistent with rolling-hinge style flexure of the footwall.

Abstract

Quantifying lithospheric strength is essential to better understand seismicity in continental regions. We estimate differential stresses and principal stress orientations driving rapid slip (~10 mm/yr) on the active Mai'iu low-angle normal fault in Papua New Guinea. The fault's mafic footwall hosts a well-preserved sequence of mylonite, foliated cataclasite, ultracataclasite and gouge. In these fault rocks, we combine stress inversion of fault-slip data and paleostress analysis of syntectonically emplaced calcite veins with microstructural and clumped-isotope geothermometry to constrain a syn-exhumational sequence of deformation stresses and temperatures, and to construct a stress profile through the exhumed footwall of the Mai'iu fault. This includes: 1) at ~12–20 km depth (T≈275–370°C), mylonites accommodated slip on the Mai'iu fault at low differential stresses (>25–135 MPa) before being overprinted by localized brittle deformation at shallower depths; 2) at ~6–12 km depth (T≈130–275°C) differential stresses in the foliated cataclasites and ultracataclasites were high enough (>150 MPa) to drive slip on a mid-crustal portion of the fault (dipping 30–40°), and to trigger brittle yielding of mafic footwall rocks in a zone of mixed-mode seismic/aseismic slip; and 3) at the shallowest crustal levels (T<150°C) on the most poorly oriented part of the Mai'iu fault (dipping ~20–24°), slip occurred on frictionally weak clay-rich gouges ($\mu \approx 0.15–0.38$). Subvertical σ_1 and subhorizontal σ_3 parallel to the extension direction, with $\sigma_1 \approx \sigma_2$ (constriction), reflect vertical unloading and 3-D bending stresses during rolling-hinge style flexure of the footwall.

1 Introduction

Lithospheric or crustal strength is often expressed as the maximum differential stress that a rock can sustain before it fractures or flows. Most knowledge of brittle rock strength comes from laboratory experiments (e.g., Byerlee, 1978) and deep boreholes (e.g., Zoback & Harjes, 1997; Hickman & Zoback, 2004). These studies typically infer Coulomb frictional failure in the upper crust, in which the differential stress or shear stress (τ) is linearly related to the effective normal stress (σ_e) via a "Byerlee" coefficient of friction (μ=0.6–0.85, Byerlee, 1978; Behr & Platt, 2014). Detachment faults that may have formed and/or slipped as “low-angle normal faults” (<30°, LANFs), remain a controversial topic because Andersonian normal faults in Mohr-Coulomb materials with “Byerlee” frictional strength should initiate and slip at dips of 60–75° and frictionally lock-up at dips <30–45° (e.g., Anderson, 1951; Sibson, 1985; Lister & Davis, 1989; Collettini & Sibson, 2001; Axen, 2004, 2007; Collettini, 2011). Yet, a small number of normal faults are demonstrably active today at low angles (dip <30°; e.g., Rigo et al., 1996; Chiaraluce et al., 2007, 2014; Hreinsdóttir & Bennett, 2009; Wallace et al., 2014).

How crustal strength changes as a function of depth and whether LANFs are weak relative to their surroundings, to other faults, and to laboratory friction values remain fundamental questions in geodynamics (e.g., Axen, 2004; Behr & Platt, 2011 and references therein). Slip on a seemingly misoriented, shallow normal fault in an Andersonian stress regime might be achieved by: (1) high pore fluid pressures within the fault zone (e.g., Axen, 1992; Collettini & Barchi, 2004; Ikari et al., 2009; Abers, 2009); and/or (2) frictionally weak fault materials such as a phyllosilicate-rich (i.e., talc, saponite) gouge (e.g., Floyd et al., 2001; Collettini et al., 2009a, 2009b; Collettini, 2011; Lockner et al., 2011). A third possible mechanism for low-angle slip involves rotation of the principal stress axes to “non-Andersonian” orientations; for example, due to coseismic damage-induced changes in fault zone elastic properties, earthquake rupture dynamics, topographic loads, lateral density variations, and/or horizontal or vertical shear tractions caused by lower crustal flow (e.g., Yin, 1989 and related comments by Buck, 1990; Axen, 2004; Westaway, 2005; Faulkner et al., 2006). Finally, where the near-surface portion of a LANF is convex-up—rather than planar—mechanical resistance to slip may be much reduced (Choi & Buck, 2012; Reston, 2020).

Where they bound metamorphic core complexes (MCCs), detachment faults typically record slip magnitudes of tens of kilometres—sufficient to exhume crustal rocks in their footwall

from below the brittle-ductile transition (BDT; e.g., Whitney et al., 2013; Platt et al., 2015). Microstructural, paleopiezometric, and geothermometric data from these exhumed rocks can be combined to produce a naturally constrained profile of crustal strength with depth (e.g., Behr & Platt, 2011). Detachment faults are particularly appropriate for such an analysis, because they typically undergo progressive strain localization (e.g., Behr & Platt, 2011; Platt et al., 2015; Cooper et al., 2017) that preserves relicts of older-formed fault rocks in the structurally lower part of the exhumed fault rock sequence (Mizera et al., 2020). Most previously studied examples of MCCs are ancient, and processes that drove slip on these detachments are obscured by combinations of tectonic tilting, erosion, chemical alteration, and other post-slip overprints (e.g., Axen & Hartley, 1997; Axen, 2004; Collettini, 2011; Whitney et al., 2013); while most known active examples of LANFs are concealed beneath a cover of brittlely faulted upper-plate rocks (e.g., Rigo et al., 1996; Chiaraluce et al., 2014). Exhumed fault rocks are exposed within the ~3 km-tall domal footwall of the Mai'iu fault in SE Papua New Guinea, one of the best-preserved active continental LANFs on Earth (e.g., Wallace et al., 2014; Webber et al., 2018). Dip slip on this fault at ~10 mm/yr for the past 3–4 Myrs (Wallace et al., 2014; Webber et al., 2018; Österle et al., 2020) has exhumed a >29 km-wide, little-eroded fault surface in its metabasaltic footwall. Along—and immediately beneath—this fault surface, freshly exhumed microstructures in the host metabasalt are well-preserved (Little et al., 2019; Mizera et al., 2020).

In this study, we compile stress-depth snapshots by taking advantage of space-for-time relationships provided by progressive slip localization within the cooling and exhuming footwall of the Mai'iu fault. Estimated differential stresses are based on the mechanical twinning and/or recrystallized grain-size of deformed calcite veins that cross-cut the sequentially formed fault rock units. Deformation temperatures are based on a combination of calcite microstructures (i.e., calcite-twin morphologies; Ferrill et al., 2004), clumped isotopes in calcite (Stolper & Eiler, 2015) and chlorite-composition geothermometry (Cathelineau, 1988; Bourdelle & Cathelineau, 2015). We invert for the orientation of principal stresses acting on the fault zone using two datasets: crystallographic data for calcite-twins collected by electron backscatter diffraction, and fault-slip data of late outcrop-scale brittle faults cross-cutting the footwall and hangingwall of the Mai'iu fault. By applying paleostress and geothermometric methods to the sampled fault rock sequence, we reconstruct differential stresses, temperatures and principal stress orientations along the exhumation path of the fault. These datasets are used to infer a stress profile along the

Mai'iu fault, from which we derive the fault's peak strength and the integrated strength of the extending brittle crust (see Supporting Information S1 for a detailed explanation of this concept).

2 The Suckling-Dayman Metamorphic Core Complex

The tectonic regime in SE Papua New Guinea is governed by the oblique-convergent motion of the Pacific (PAC) and Australian plates (AUS) at ~100–110 mm/yr (Figure 1a). This collisional motion is absorbed across an intervening mosaic of microplates (Tregoning et al., 1998; Wallace et al., 2004, 2014). Present-day counterclockwise rotation of the Woodlark-Solomon Sea microplate at 2–2.7°/Myr relative to Australia is accompanied by 20–40 mm/yr of seafloor spreading in the oceanic Woodlark Basin and, farther west, by 10–15 mm/yr of extension across the continental Woodlark rift (Wallace et al., 2004). Extension in the Woodlark rift initiated sometime in the interval 3.6–8.4 Ma (Taylor & Huchon, 2002; Little et al., 2007, 2011; Fitz & Mann, 2013). Extension near the western end of the Woodlark rift is accommodated primarily by slip on the Mai'iu fault. There, cosmogenic nuclide concentrations from the exposed Mai'iu fault scarp indicate a late Holocene dip-slip rate of 11.7±3.5 mm/yr (Webber et al., 2018), and geodetic data confirm a present-day dip-slip rate of 7.5–10.2 mm/yr (Wallace et al., 2014; Biemiller et al., 2020).

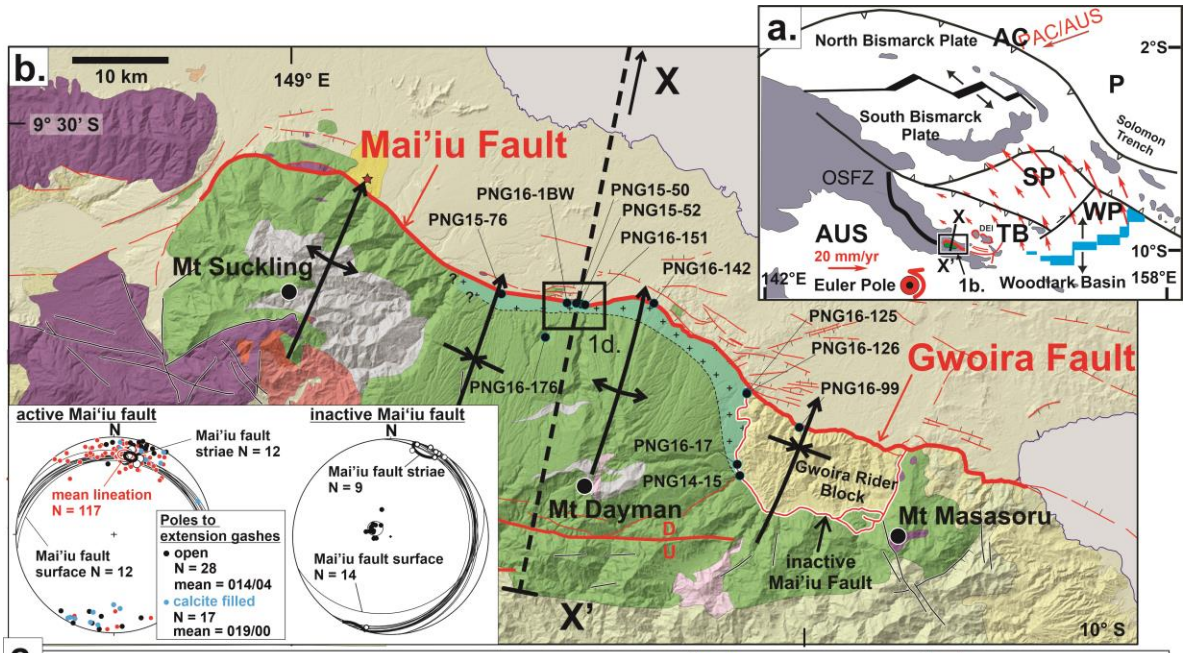
a.
North Bismarck Plate
AC
AC/AUS
2°S
P
South Bismarck Plate
Solomon Trench
OSFZ
SP
WP
AUS
20 mm/yr
Euler Pole
TB
10°S
142°E
158°E
Woodlark Basin
1b.
b.
10 km
149° E
9° 30' S
Mai'iu Fault
Mt Suckling
PNG16-1BW
PNG15-50
PNG15-52
PNG15-76
PNG16-151
PNG16-142
1d.
PNG16-125
PNG16-126
Gwoira Fault
PNG16-176
PNG16-99
PNG16-17
PNG14-15
Gwoira Rider Block
Mt Dayman
Mt Masasoru
inactive Mai'iu Fault
10° S
active Mai'iu fault
Mai'iu fault striae N = 12
mean lineation N = 117
Mai'iu fault surface N = 12
Poles to extension gashes
open N = 28 mean = 014/04
calcite filled N = 17 mean = 019/00
inactive Mai'iu fault
Mai'iu fault striae N = 9
Mai'iu fault surface N = 14

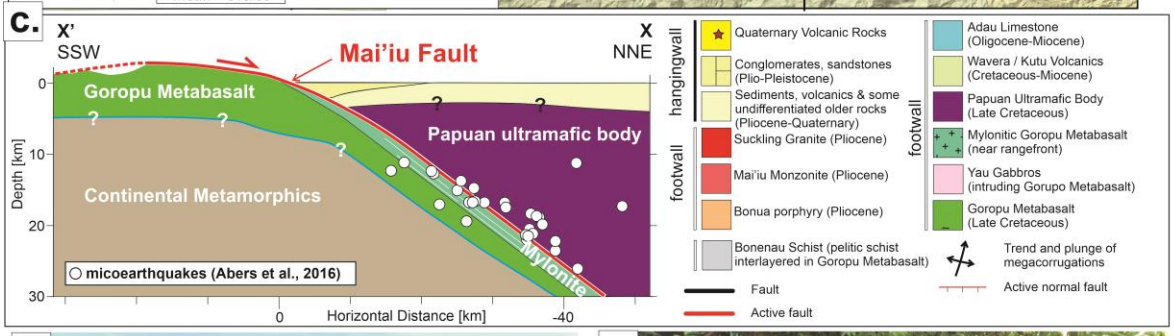
c.
X'
SSW
X
NNE
Mai'iu Fault
Goropu Metabasalt
Papuan ultramafic body
Continental Metamorphics
Mylonite
micoearthquakes (Abers et al., 2016)
Depth [km]
Horizontal Distance [km]
hangingwall
footwall
Quaternary Volcanic Rocks
Conglomerates, sandstones (Plio-Pleistocene)
Sediments, volcanics & some undifferentiated older rocks (Pliocene-Quaternary)
Suckling Granite (Pliocene)
Mai'iu Monzonite (Pliocene)
Bonua porphyry (Pliocene)
Bonenau Schist (pelitic schist interlayered in Goropu Metabasalt)
Adau Limestone (Oligocene-Miocene)
Wavera / Kutu Volcanics (Cretaceous-Miocene)
Papuan Ultramafic Body (Late Cretaceous)
Mylonitic Goropu Metabasalt (near rangefront)
Yau Gabbros (intruding Gorupo Metabasalt)
Goropu Metabasalt (Late Cretaceous)
Trend and plunge of megacorrugations
Fault
Active fault
Active normal fault

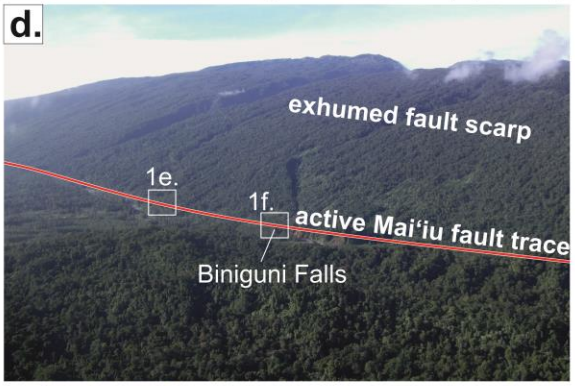
d.
exhumed fault scarp
1e.
1f.
active Mai'iu fault trace
Biniguni Falls


e.
exhumed fault surface
50 cm

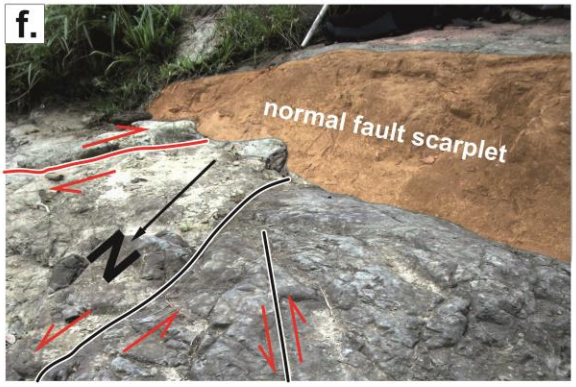
f.
normal fault scarplet

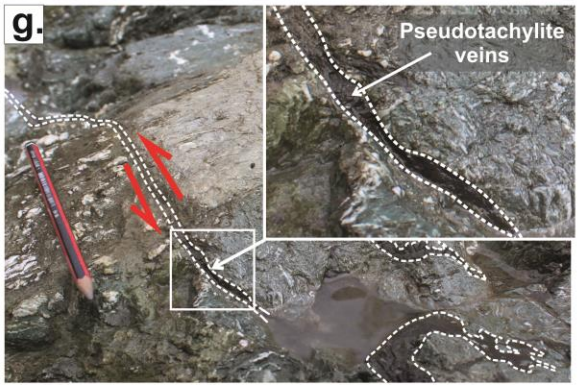
g.
Pseudotachylite veins

Figure 1. a) Simplified tectonic map of the Woodlark Rift (after Wallace et al., 2004). Locations of Figure 1b and cross-section X-X' of Figure 1c are highlighted. b) Geological and structural map of the Suckling-Dayman Metamorphic Core Complex (after Smith & Davies, 1976; Lindley et al., 2014; Little et al., 2019). Sample locations for this study (black dots) are labelled on this map (e.g., "PNG16-126"). Inset, lower-hemisphere, equal-area stereograms of fault kinematic data collected in the mylonitic footwall of the Mai'iu fault <300 m up-dip from its trace: left stereogram, measured attitudes of the Mai'iu fault surface (black great circles), trend and plunge of wear striae on the Mai'iu fault surface (white dots) and mylonitic lineation (red dots), poles of extension gashes that are either open (black dots) or filled with calcite (light blue dots); right stereogram, attitudes of a now inactive part of the Mai'iu fault that has been tilted eastward on the limb of the synclinally folded Gwoira rider block at location PNG16-17 (black great circles); trend and plunge of wear striae on the Mai'iu fault at this location (white dots) are also shown. c) Tectonic cross-section of the Mai'iu fault (after Little et al., 2019). Microearthquake foci (open white dots) are based on Abers et al. (2016). d) Oblique aerial photograph of the active Mai'iu fault rangefront scarp covered in rainforest looking SE. For location see box in part b). e) Youngest, most recently exhumed surface of the active Mai'iu fault at the base of its scarp (PNG15-50). f) Outcrop photograph (PNG16-1BW) showing the exhumed mylonitic footwall of the Mai'iu fault cross-cut by a dip-slip normal fault (orange shading) and dextral and sinistral strike-slip faults. g) Outcrop photograph of the foliated cataclasite exposed in the footwall of the E-tilted, inactive part of the Mai'iu fault trace (PNG16-17). Inset shows a sinistral strike slip fault with pseudotachylite on the slip surface. PAC—Pacific plate; AUS—Australian plate; WP—Woodlark plate; SP—Solomon-Sea plate; TB—Trobriand block; DEI—D'Entrecasteaux Islands; OSFZ—Owen-Stanley Fault Zone.

The Mai'iu fault bounds the Suckling-Dayman Metamorphic Core Complex (SDMCC, Figure 1b). Wear striae preserved on the Mai'iu fault surface trend 009–015° (Figure 1b, inset), subparallel to the current velocity of the Woodlark-Solomon Sea microplate relative to Australia as derived from elastic block modelling of campaign GPS data (Wallace et al., 2014), and to the trend of numerous corrugations in the footwall of the SDMCC (Spencer, 2010; Daczko et al., 2011; Little et al., 2019; Mizera et al., 2019). On average, the Mai'iu fault dips ~22±2° to the NNE where it emerges from the Holocene alluvial gravel of its hangingwall, and locally it dips

as little as ~16° at the surface (Figure 1b, inset). Downdip of the surface trace, and aligned with it, microearthquake foci scattered between 12 and 25 km depth define an actively slipping deformation zone dipping north at 30–40° (Figure 1c; Abers et al., 2016). This deformation zone is interpreted as the subsurface continuation of the Mai'iu fault (Abers et al., 2016; Little et al., 2019). The Mai'iu fault is thought to have extensionally reactivated part of the Owen-Stanley thrust—a Late Cretaceous-Paleocene subduction thrust (Webb et al., 2008; Daczko et al., 2011). The Owen-Stanley thrust formed during the obduction of an oceanic and island arc upper plate (the Late-Cretaceous Papuan Ultramafic Belt; PUB) over an oceanic marginal basin and Australian Plate-allied continental margin rocks (Davies, 1978; Webb et al., 2008; Daczko et al., 2009). The Mai'iu fault footwall consists of MORB-derived metabasaltic rocks of >3–4 km thickness with minor interbedded phyllitic metasediments, limestone and chert, known as the Goropu Metabasalt (Figure 1b; Smith & Davies, 1976).

To the east of the SDMCC at location PNG16-17 (Figure 1b, inset), an inferred inactive part of the Mai'iu fault dips 16±3° to the ESE and is overlain by a fault slice of the Plio-Pleistocene Gwoira Conglomerate. This slice of former hangingwall comprises a rider block (following Choi & Buck, 2012; Reston, 2020) that formed when part of the Mai'iu fault was abandoned upon inception of a younger and more steeply dipping splay of the Mai'iu fault called the Gwoira fault (Webber et al., 2020). The dips of sedimentary growth strata in the rider block and tilting of a flight of late Quaternary fluvial terraces record progressive synclinal folding and southward back-tilting of the rider block, some of which continues today (Mizera et al., 2019; Webber et al., 2020).

2.1 Mai'iu Fault Rocks

The footwall of the Mai'iu fault exposes a self-exhumed sequence of mostly mafic-composition fault rocks (Figures 1d and 1e; in detailed described in Little et al., 2019, Mizera et al., 2020, and Biemiller et al., 2020). From bottom to top, they include: a) nonmylonitic greenschist (protolith); b) mylonite (derived from the protolith); c) foliated cataclasite; d) ultracataclasite; and e) saponite-rich gouge. The fault rocks contain multiple generations of deformed calcite veins, except for the gouge layer, which contains only broken, reworked fragments of former calcite and dolomite veins (Mizera et al., 2020).

The mylonite unit (mylonites) is at least 60 m thick along the northern active rangefront, thinning southward to as little as 1.5 m farther up-dip of the frontal trace (at location PNG16-17, Fig. 1b). The mylonitic rocks are LS-tectonites with a well-defined NNE-trending stretching lineation and late Neogene, normal-sense shear fabrics. Based on pseudosection modelling of their mineral assemblage (epidote, actinolite, chlorite, albite, titanite, ±quartz, ±calcite), the mylonites are inferred to have been exhumed from ~25±5 km depth with peak metamorphic temperatures of 425±50°C and pressures of 5.9–7.2 kbar (Daczko et al., 2009). Well-exposed on the exhumed fault surface immediately south of the fault trace, small-offset (slip <1.5 m) brittle faults cross-cut the fault surface and mylonites. These faults comprise: a) steep, 50°–75° down-to-the-north dipping, synthetic normal faults; and b) near-vertical strike-slip faults (Figure 1f; Supporting Information S2). The latter occur as a conjugate set of ENE-striking dextral and NW-striking sinistral faults that mutually cross-cut one another. Steeply-dipping, late-stage extension (to mixed shear-extension) gashes cross-cut the mylonites at a high angle to the foliation and strike nearly orthogonal to both the direction of fault slip and the mean trend of mylonitic lineations (Figure 1b, inset). In the rider block, sedimentary beds of the Gwoira Conglomerate are cross-cut by mostly moderate to steeply dipping normal faults that dip variably to the north and south (Supporting Information S2).

The mylonites were overprinted and reworked into a structurally overlying, ~3–1.5 m thick foliated cataclasite unit (foliated cataclasites). The cm- to mm-spaced foliation in the foliated cataclasites is defined by light-coloured albite and quartz±calcite-rich domains and darker phyllosilicate (predominantly chlorite)-rich folia. Meter-to-micro-scale normal and strike-slip faults are more densely developed—but less systematically oriented—in the foliated cataclasites (Supporting Information S2). Figure 1g shows a sinistral strike-slip fault that is coated with an inferred pseudotachylite vein. Multiple generations of such black-colored, ultra-fine-grained veins up to 40 mm-thick cross-cut the foliated cataclasites, in some cases with clear injection features. Five pseudotachylite samples with confirmed glassy matrices were dated by $^{40}Ar/^{39}Ar$ geochronology; the ages (interpreted as minimum ages for friction melting) range from 2.24±0.29 Ma to 3.00±0.43 Ma (Little et al., 2019).

The foliated cataclasites are structurally overlain by a ~5–40 cm thick ultracataclasite unit (ultracataclasites; Figure 1e). The ultracataclasites contain remnant mafic minerals and older (recycled) ultracataclasite fragments embedded in a clay-rich (predominantly corrensite and/or

saponite) matrix. The ultracataclasites are sharply overlain by one or more layers of incohesive saponite-rich gouge up to 12 cm thick. The upwardly-thinning arrangement of progressively lower-temperature-formed fault rock units, each of which reworks the subadjacent rocks, is interpreted as a strain-localizing time sequence (Little et al., 2019; Mizera et al., 2020). In the rider block, a sharp, planar slip surface places the unmetamorphosed Gwoira Conglomerate (former hangingwall) against the saponite-rich gouge. Clasts in the Gwoira Conglomerate are cemented by calcite.

3 Methods

3.1 Structural Measurements, Thin Section Preparation and Microstructural Analysis

Structural measurements and fault rock samples were collected in the footwall and former hangingwall (Gwoira Conglomerate) of the Mai'iu fault (sample locations in Figure 1b). Samples were cut parallel to lineation (or wear striae) and perpendicular to foliation. An optical microscope was used to identify calcite veins in over 100 thin sections. We selected a representative suite of 15 samples spanning the several fault rock units to be prepared into ultrapolished sections. These samples were polished with diamond paste and SYTON (silica suspension; Fynn & Powell, 1979). Fragile specimens were dried for 24 hours at 50°C and impregnated with epoxy prior to polishing.

Calcite microstructures in polished sections were analysed with a SIGMA-VP field emission gun scanning electron microscope (FEG-SEM) equipped with an electron backscatter diffraction (EBSD) detector at the University of Otago, using 30 kV acceleration voltage, 50–100 nA beam current, 20–30 mm working distance and 70° sample tilt. Electron backscatter patterns were collected by an HKL Nordlys camera and processed and indexed with the AZTEC software by Oxford Instruments. To resolve the microstructures of calcite veins, step sizes of 0.2–1.5 µm were used.

3.2 Paleostress Analysis

Calcite twinning paleopiezometry

Mechanical twinning on e-planes $\{01\bar{1}8\}$ (using hexagonal structural cell indices) in calcite, for which the shear displacement is in the direction $\langle 0\bar{2}21\rangle^{+}$ (positive sense; Barber & Wenk, 1979; De Bresser & Spiers, 1997), is the result of crystal-plastic deformation at

244 temperatures below 400°C (Groshong, 1988). E-twinning in calcite depends on the orientation of
245 stress and attainment of the critical resolved shear stress (CRSS; 2–12 MPa) along the shear
246 direction on any of the three symmetrically equivalent lattice e-planes (e.g., Jamison & Spang,
247 1976; Tullis, 1980; Burkhard, 1993; Lacombe & Laurent, 1996; Yamaji, 2015). The e-twin
248 density in a calcite grain is dependent on differential stress and independent of grain size (Rowe
249 & Rutter, 1990; Rybacki et al., 2013; Brandstätter et al., 2017). The width of a calcite e-twin is
250 mainly a function of temperature and is only weakly dependent on strain, strain rate or stress
251 (e.g, Rowe & Rutter, 1990; Burkhard, 1993; Ferrill et al., 2004). Twin morphology can provide a
252 rough estimate of deformation temperature (Burkhard, 1993; Ferrill et al., 2004).
253 Crystallographic orientation data for adjoining calcite-twin pairs in calcite veins cross-
254 cutting the Mai'iu fault rocks were collected and mapped using EBSD. For each calcite grain, we
255 measured: a) the width of e-twins; and b) the twin density. The latter was determined by
256 counting the number of e-twin lamellae of a given twin set perpendicular to the twin boundaries
257 of individual grains normalized to a unit length of 1 mm (Rybacki et al., 2011; Supporting
258 Information S3). Differential stresses were estimated using the experimentally calibrated twin-
259 density paleopiezometer of Rybacki et al. (2013):

260 $$\sigma_{Diff} = (19.5 \pm 9.8)\sqrt{N_L}, \qquad \text{(Eq. 1)}$$

261 where N_L is the number of e-twins per mm. This paleopiezometer employs conditions relevant to
262 medium to lower greenschist-facies rocks (>20 to 350°C) that have been deformed to high
263 strains, and is thus best-suited to the calcite veins in our study. For comparison, results from this
264 and two other twin-density paleopiezometers are shown in Supporting Information S3.
265
266 *Recrystallized grain-size paleopiezometry*
267 Dynamic recrystallization of calcite may occur at deformation temperatures >250°C (e.g.,
268 Evan & Dunne, 1991: Weber et al., 2001). The mean recrystallized grain size of calcite is a
269 function of differential stress and can be measured from EBSD maps (e.g., Valcke et al., 2015).
270 We followed the EBSD-based procedure of Cross et al. (2017) to measure calcite grain sizes in
271 veins cross-cutting the Mai'iu fault rocks, and to identify the subset of grains that are
272 recrystallized (detailed description in Supporting Information S4). Differential stresses were then
273 calculated from the average grain size of recrystallized calcite using the paleopiezometer

calibrations by Valcke et al. (2015; $K_{EBSD}=10^{1.9\pm0.2}$; $p_{EBSD}=-0.6\pm0.1$), and Platt and De Bresser (2017; $K_{OPT}=10^{3.1\pm0.3}$; $p_{OPT}=-1.09(+0.14; -0.18)$):

$$D_X = K_X \cdot {\sigma_{Diff}}^{-p_X}, \quad \text{(Eq. 2)}$$

where D_X is the average grain size, K_X and p_X are constants. Calculated differential stresses with both paleopiezometers by Valcke et al. (2015) and Platt and De Bresser (2017) are shown in Supporting Information S4.

Principal Stress Orientations

Fault slip data (fault attitude, striation direction, sense of slip) were collected in the field for 54 brittle faults cutting the ~20–24°-dipping exhumed plane of the active Mai'iu fault within the mylonites and foliated cataclasites near the base of the fault scarp (<300 m updip of the trace) at 8 locations, and for 30 brittle faults cutting the sedimentary beds of the Gwoira Conglomerate at 21 locations across the rider block. Markers indicating sense of offset included the exhumed surface of the Mai'iu fault (footwall), bedding in the Gwoira Conglomerate (hangingwall), and steeply dipping quartz or calcite veins (best for strike-slip faults cutting the exhumed footwall). Slip directions were inferred from wear striae or calcite fibres (fault surface veins). The fault kinematic data were inverted to determine best-fit orientations of principal stress axes (σ_1 and σ_3) and the stress ratio (Φ), where

$$\Phi = \frac{(\sigma_2-\sigma_3)}{(\sigma_1-\sigma_3)}. \quad \text{(Eq. 3)}$$

By definition, the stress ratio (Φ) is 0 for $\sigma_1 > \sigma_2 = \sigma_3$ (axial compression) and 1 for $\sigma_1 = \sigma_2 > \sigma_3$ (axial constriction).

Calcite-twin data (pairs of adjacent twinned and untwinned c-axis crystallographic orientations from EBSD analysis) were also used to invert for paleostress directions. The twinning data were recast into a form analagous to fault-slip data using the following steps (e.g., Turner, 1962; Groshong, 1975; Engelder, 1979; Kilsdonk & Wiltschko, 1988; Craddock & Magloughlin, 2005; Jaya & Nishikawa, 2013; Kanai & Takagi, 2016): 1) crystallographic orientation data from host calcite grains (N=912) and their adjacent e-twins (N=3937) were collected by EBSD; 2) the crystallographic orientations from the e-twin and the host calcite grains were used to determine the e-twin plane, glide direction, and sense of shear for every twin pair based on the known angular relationships (e.g., Burkhard, 1993); and 3) the kinematic data (glide plane, direction, and shear sense) were converted from a sample coordinate system

(relative to lineation, foliation, and top-bottom) to a geographical one (N–S, E–W, and top–bottom; see Data Repository for the conversion MATLAB-code).

To analyse both of the above datasets, we use the multiple inverse method (MIM) by Yamaji (2000) to invert the kinematic observations for best-fit stress orientations and values of the stress ratio parameter, Φ (Eq. 3). For the calcite-twin data, we compare the results of the Yamaji (2000) algorithm with those of three other tensor inversion techniques applied to calcite twinning data (P-, B- and T-axes calculations after Turner, 1953; strain-gage technique after Groshong 1972, 1974; dihedra calculation after Angelier & Mechler, 1977; see Tables S5.1 and S5.2 in Supporting Information S5). All of them yielded statistically indistinguishable best-fit stress orientations (Supporting Information Figure S5). An advantage of the MIM is that it self-correlates fault-slip data by dividing a set of faults into subsets that might represent the component stress field acting on that subset of the data. The number of subsets equals the binomial coefficient ${}_{N}C_{k}=N!/k!(N–k)!$, where N is the total number of fault-slip (or calcite twin) data and k the number of elements comprising a subset. The value k is recommended to be 4 or 5 (Yamaji, 2000). The reliability of this method depends on the number of collected data, the spatial or temporal heterogeneity of the stress state and the number of subsets that can be correlated to one another (Yamaji, 2000; Otsubo & Yamaji, 2006; Otsubo et al. 2008).

3.3 Clumped-isotope Geothermometry of Calcite

Carbonate ‘clumped isotopes’ are utilized to reconstruct past formation temperatures in carbonate minerals based on the temperature dependent ordering of ^{13}C and ^{18}O atoms into bonds with each other in the same carbonate molecule (Ghosh et al., 2006; Eiler, 2011). We analyzed 18 calcite samples from the Mai’iu fault footwall and two calcite cement samples from the Gwoira Conglomerate for carbon, oxygen and clumped isotopes. Analyses were performed on 7–12 mg of individual aliquots of reference materials and unknown calcite samples at Caltech using previously established procedures (Ghosh et al., 2006; Huntington et al., 2009; Passey et al., 2010; Dennis & Schrag, 2010). Briefly, the carbonate materials were digested in phosphoric acid at 90°C to produce CO_2. The CO_2 was purified from H_2O, trace organics and other contaminants by using a dry ice/ethanol trap and a gas chromatograph with a Porapak Q 120/80 mesh column held at -20°C. The resulting CO_2 was purified again using dry ice/ethanol and nitrogen traps and introduced into a dual inlet Finnigan MAT-253 mass spectrometer. Masses 44–48 were

simultaneously collected to obtain Δ_{47}, Δ_{48}, $\delta^{13}C$ and $\delta^{18}O$ values. We define R^{47} as the abundance of mass 47 isotopologues divided by the mass 44 isotopologue. Δ_{4x} is reported relative to a stochastic distribution of isotopologues for the same bulk isotopic composition. For example, Δ_{47} is equal to $(((R^{47}_{measured}/R^{47}_{stochastic})-1)-((R^{46}_{measured}/R^{46}_{stochastic})-1)-((R^{45}_{measured}/R^{45}_{stochastic})-1))*1000$. Δ_{48} was monitored to detect any hydrocarbon contamination. Measurements of each gas were done at 16V of mass 44 and consisted of 8 acquisitions, each of which involved 7 cycles of sample-standard comparison with an ion integration time of 26s per cycle. Internal standard errors for Δ_{47} averaged 0.02‰.

$\delta^{13}C_{VPDB}$ and $\delta^{18}O_{VSMOW}$ values of samples and standards were calculated from raw ion currents of mass 44–46 using "Brand" parameters (Brand et al., 2010). The Δ_{47} raw data was corrected for instrument nonlinearity and scale compression (Passey et al., 2010). Several heated and equilibrated gases of various bulk isotopic compositions were run during each session. These gases were then used to convert measurements into the interlaborartory absolute reference frame (ARF; Dennis & Schrag, 2010). Finally, $\Delta_{47,ARF}$ was converted to temperature using the Bonifacie calibration (Bonifacie et al., 2017).

4 Results

4.1 Paleostresses and Deformation Temperatures Based on Calcite Veins

Field and microstructural description of the calcite veins

Most calcite veins cross-cutting the mylonites and subjacent nonmylonitic schists are oriented subperpendicular to the foliation (Figure 2a). In the mylonites, some veins are disposed at shallower angles and appear to have been deformed away from that originally steep attitude as a result of top-to-the-north shearing. These latter veins are commonly cross-cut by younger, less deformed veins that remain more nearly foliation-orthogonal. Calcite veins in the mylonites usually contain large, up to 1 mm-sized (long axis of grain), twinned grains that are surrounded by fine, 5–20 μm-sized, untwinned calcite grains ("core and mantle" microstructure; Figures 2b–2e). Grain boundaries of the larger grains are usually interlobate and bulged at a wavelength that is similar to the size of the finer calcite grains (Figure 2c), suggesting dynamic recrystallization by subgrain rotation recrystallization. In two-dimensional EBSD maps, the long axes of the recrystallized grains are oriented oblique (~30°) to the mylonitic foliation (Figure 2e, inset) and

364 define a weak shape-preferred orientation (SPO). Calcite twins in the larger calcite grains are
365 thick and patchy, bent, twinned, and have sutured twin boundaries (Figures 2b and 2c). The veins
366 also contain single twin boundaries that bulge into the untwinned crystal and merge with other
367 twins within the same calcite grain. These twin morphologies resemble Type IV and Type III
368 twins of Burkhard (1993) consistent with deformation at temperatures >250–400°C (e.g., Evans
369 & Dunne, 1991; Ferrill et al., 2004). Some calcite veins contain ~200 μm-sized calcite grains
370 with up to ~3 μm-thick twins (Figure 2a, inset), resembling Type III and Type II twins of
371 Burkhard (1993) that may record a lower deformation temperature (~200–300°C) conditions
372 (Groshong et al., 1984; Evans & Dunne, 1991; Ferrill et al., 2004).
373

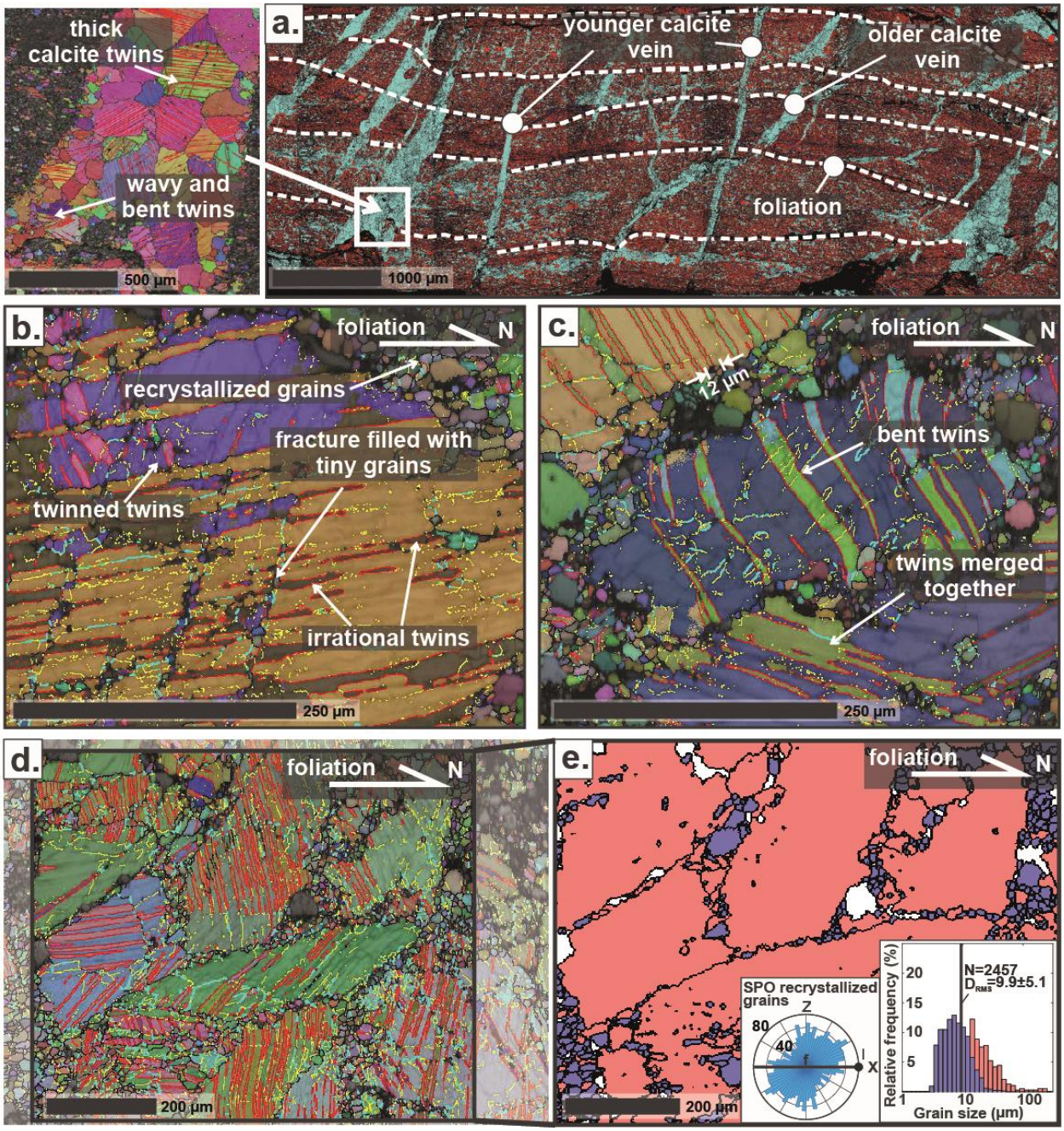

Figure 2. Representative EBSD-based microstructural images of calcite veins in nonmylonitic schist (sample PNG14-15 in part a.) and in mylonite (sample PNG16-1BW in parts b. through e.). The normal (top-to-the-north) slip sense of the Mai'iu fault is shown as top-to-the-right. a) Phase map of nonmylonitic metapelitic schist from ~3 m below the fault trace, containing multiple generations of calcite veins; older, more deformed grains are oblique to the foliation (more sheared). Phases: light blue—calcite; red—quartz; white dashed lines—foliation. Inset on left: enlargement of deformed calcite vein containing twinned grains. b) All Euler color map of a

large (~1 mm) calcite grain surrounded by fine calcite grains. Several twins (~25 µm-wide) are internally twinned. c) All Euler color map of large (~300 µm) calcite grains surrounded by fine calcite grains. Large calcite grains show bent twins and twin boundaries that merge with other twins in the same host grain. d) All Euler color map showing several large calcite grains with thick twins and fine-grained calcite at the grain boundaries of the larger grains. e) Map of relict (red) and inferred recrystallized (blue) calcite grains (area investigated shown in d.). Rose diagram (inset) shows a weak recrystallized calcite grain shape-preferred orientation. Grain size histogram of relict (red) and recrystallized (rex; blue) grains of map shown in e. D_{RMS}—mean (root mean square) recrystallized grain size. Color code for crystallographic misorientation of boundaries in a. (inset), b., c. and d. are: yellow 2–5°, light blue 5–10°, black >10° (grain boundaries), red 77±5° (twins).

The foliated cataclasites host multiple generations of calcite veins that have mutually cross-cutting relationships with respect to local ultracataclasite seams and inferred pseudotachylite veins (Figure 3a; see also Little et al., 2019). The calcite veins are µm- to ≤5 mm thick and are generally oriented either suborthogonal or subparallel to the shallow (N-dipping) foliation. Backward-inclined gash veins with respect to the normal sense of shear are microfolded, whereas forward-inclined ones have been stretched and show necking structures, a relationship attributed to normal-sense ductile shearing (Figure 3b). The calcite veins typically consist of ~30–100 µm-sized, almost fully-twinned calcite grains containing predominantly ~0.5–2 µm wide, straight twins (Figure 3b, inset). These resemble Type II and Type I twins of Burkhard (1993), and suggest deformation temperatures of ~150–300°C (e.g., Evans & Dunne, 1991; Ferrill et al., 2004). Some calcite veins contain very fine-grained calcite with a grain size of ~3–15 µm (Figures 3c–3e). Larger calcite grains with a grain size of ~20–50 µm have bulged grain boundaries at a wavelength of ~4–12 µm and usually contain more abundant twins (~0.5–3 µm-wide) than the surrounding finer grains. The finer calcite grains typically form quadruple grain boundary junctions as well as straight grain-boundaries with neighbouring calcite grains; these grains are inferred to be recrystallized. The long axes of the recrystallized grains are slightly oblique (~16°) to the spaced foliation of the foliated cataclasites and define a strong SPO (Figure 3e).

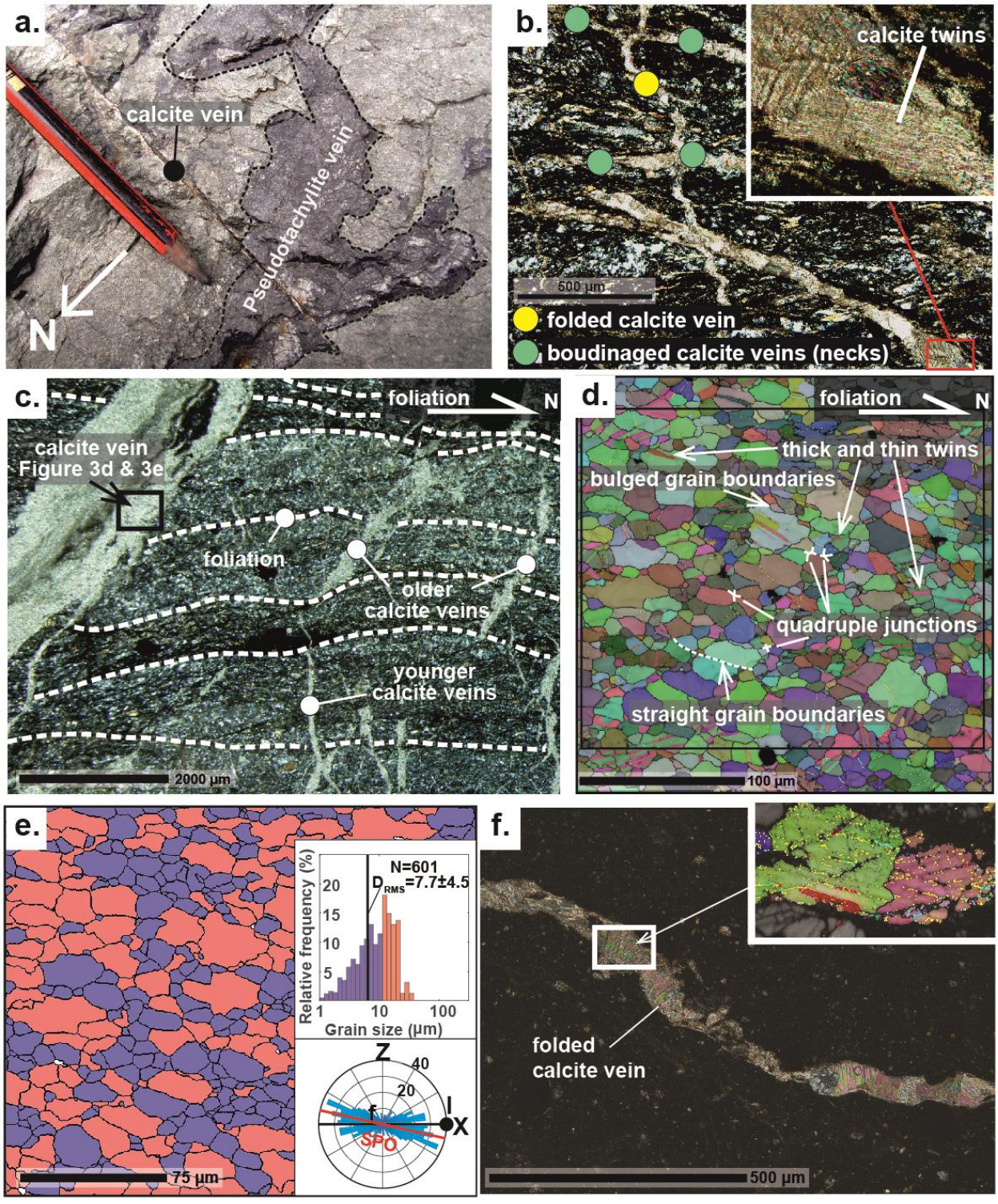

Figure 3. Microstructural observations of calcite veins in foliated cataclasites and ultracataclasites. Images are arranged with the top-to-the-north (normal) slip sense of the Mai'iu fault shown as top-to-the-right (except in a.). a) Fault-exhumed exposure of foliated cataclasite

and a pseudotachylite vein cross-cut by a mm-thick calcite vein just south (<5 m) of the active fault trace. b) Optical photomicrograph (crossed polarizers) of foliated cataclasite containing multiple calcite veins (PNG16-125B). Inset, calcite veins contain 50 to 100 µm-sized calcite grains that are almost fully twinned. Yellow dots—shortened and microfolded calcite veins; green dots—stretched calcite veins showing necking structures. c) Optical photomicrograph (crossed polarizers) showing the fine-grained mafic matrix of a foliated cataclasite cross-cut by multiple generations of calcite veins (PNG16-151E). Older calcite veins are more deformed and forward-inclined than the thinner, younger veins. White dashed lines—traces of foliation. d) All Euler angle colouring map of a calcite vein segment in foliated cataclasite (area shown in c.). Boundary misorientations are coded as follows: black >10° (grain boundaries), red 77°±5° (twins). e) Map of relict (red) and recrystallized (blue) calcite grains. Insets, top: grain-size histogram of relict (red) and recrystallized (rex; blue) grains of map d. Average grain size (root mean square; D_{RMS}) is given for the recrystallized grains; bottom: rose diagram showing a shape-preferred orientation (SPO) of recrystallized calcite grains. f) Optical photomicrograph of calcite vein in ultracataclasite (crossed polarizers). Inset, all euler angle colouring map of a calcite vein segment (same boundary misorientation coding as d.).

The ultracataclasites host ~100 µm-thick calcite veinlets (Figure 3f). Backwards-inclined veinlets with respect to the shear sense of the Mai'iu fault are microfolded, whereas those which are forward-inclined are planar, like the ones described in the foliated cataclasites. The calcite veins consists of ~50–100 µm-sized calcite grains that usually contain predominantly <1 µm-thin twins (Figure 3f, inset) suggesting that deformation of these veins was mainly accommodated by twinning. The twin morphologies match the Type I twins of Burkhard (1993) and indicate deformation temperatures of ≤170°C (e.g., Groshong et al., 1984; Ferrill et al., 2004).

Estimated differential stresses and deformation temperatures

The grain size of recrystallized calcite in deformed veins cross-cutting the mylonites and foliated cataclasites was used to estimate differential stresses (Figure 4a). The EBSD-based estimated two-dimensional mean grain sizes (root mean square, RMS) of recrystallized calcite grains in mylonites range from 21±14 µm (N=288, 1σ; PNG16-125D) to 9±5 µm (N=3465, 1σ; PNG16-142C) yielding average differential stresses of ~28±14 MPa to ~70±21 MPa,

447 respectively. Mean recrystallized grain sizes in the foliated cataclasites range from 9±4 μm
448 (N=892, 1σ; PNG16-151C) to 7±4 μm (N=1558, 1σ; PNG16-17E) indicating average differential
449 stresses in that unit ranging from ~68±23 MPa to ~110±14 MPa, respectively.
450 Calcite e-twins show a decrease in mean twin width and an increase in the mean twin
451 density as the mylonites and subjacent schists (3.4±2.2 μm twin width, 1σ; ~36±22 twins/mm,
452 1σ) transition structurally upwards into the foliated cataclasites and ultracataclasites (1.8±1.0 μm
453 twin width, 1σ; ~72±33 twins/mm, 1σ). The estimated twin densities and the twin widths are
454 consistent with a decrease in deformation temperature from >170°C in the mylonites and schists
455 to <170–200°C in the foliated cataclasites and ultracataclasites (Figure 4b). Differential stresses
456 based on mean twin densities (Figure 4c) range between 80–135 MPa (mean 110±34 MPa) in the
457 mylonites and subjacent schists to 140–185 MPa (mean 157±36 MPa) in the foliated cataclasites
458 and ultracataclasites. Although foliated cataclasite sample PNG15-50RD yielded a high
459 differential stress estimate of 229±47 MPa, we determined that pervasive intragranular fracturing
460 affected this estimate. Thus, sample PNG15-50RD was excluded in Figure 4.
461
462

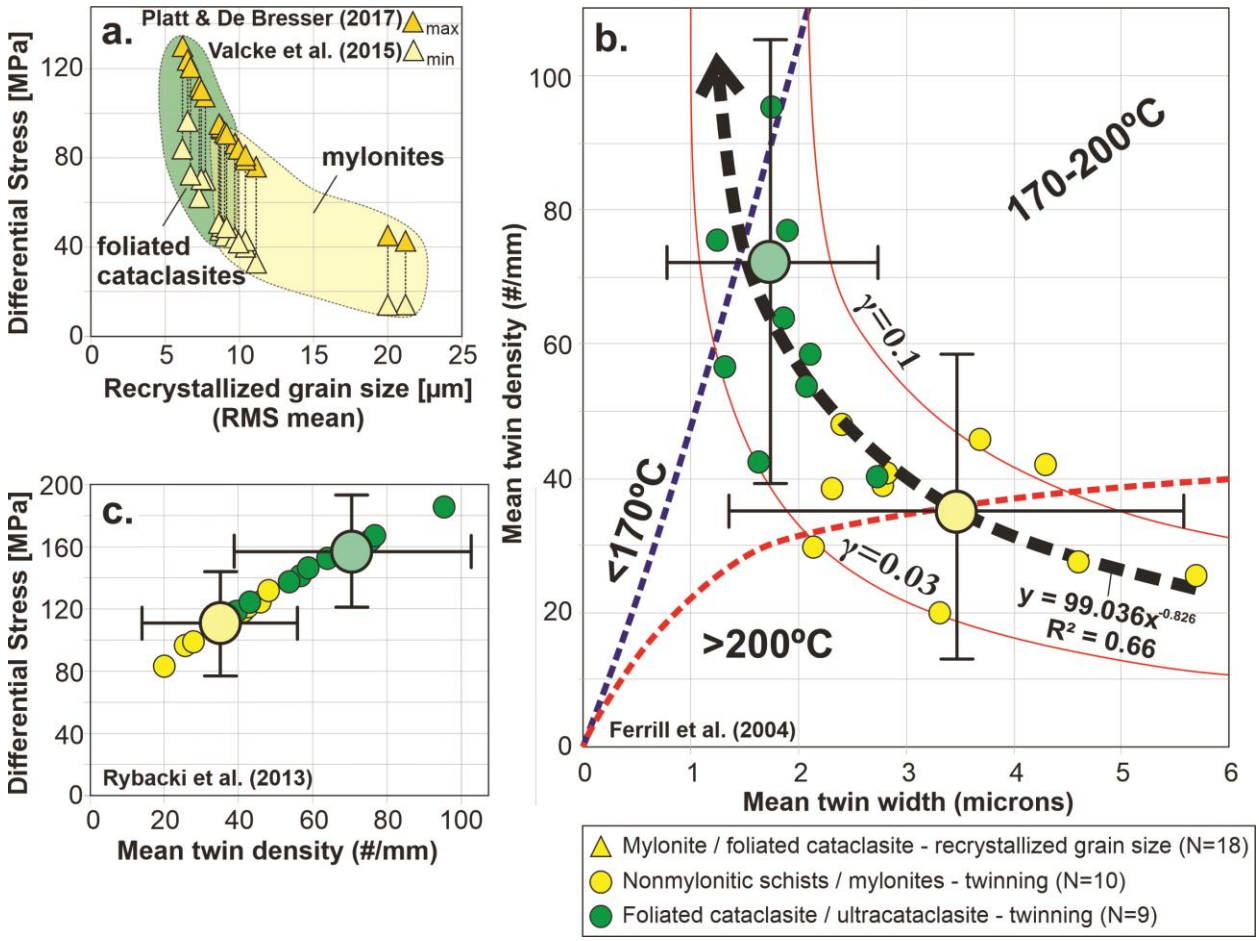

Figure 4. Estimated differential stresses and deformation temperatures of fault rocks based on calcite microstructures. a) Differential stress versus recrystallized grain size plot. b) Graph of mean twin density versus mean twin width. Dashed lines separate deformation temperature domains (after Ferrill et al., 2004). Curved red lines are isostrain magnitude contours (similar to Ferrill et al., 2004; γ—shear strain). Black arrow depicts trend of decreasing deformation temperatures in the samples representing the transition from mylonites to foliated cataclasites/ultracataclasites. Large colored circles indicate average mean twin widths and mean twin densities with average standard deviations (1σ; black bars) of mylonites and nonmylonitic schists (yellow), and foliated cataclasites and ultracataclasites (green). c) Graph of differential stress versus mean twin density. Large circles indicate average differential stresses and mean twin densities with average standard deviations (1σ; black bars) of mylonites and nonmylonitic schists (yellow), and foliated cataclasites and ultracataclasites (green).

Paleo-principal stress orientations and stress ratios based on calcite-twin slip data

Figure 5 plots solutions for best-fit principal stress axes as calculated from subsets of the calcite twin orientation data by the MIM method for veins in 10 fault rock samples. Each stress solution (tadpole) for a random subset of five calcite-twin pairs (k=5) is represented by a σ_1 (red square) and a σ_3 (blue square). The tadpole tail of each solution indicates the azimuth and plunge of the opposing principal stress axis (i.e., the σ_1-tadpole tail points in the direction of σ_3 and vice versa). Clusters of σ_1 and σ_3 represent multiple solutions with similar attitudes. The densest of these were manually grouped into oblong fields (to represent the clusters) that are shaded red or blue, as appropriate. The percentage of the data (calcite-twin pairs) that lie within each stress solution cluster (and achieve an angular misfit threshold of <30°) is labelled below the stereoplot, as is the mean stress ratio (Φ) corresponding to that cluster. For each sample, the globally averaged solution for the σ_1 and σ_3 axes, spanning all of the calcite-twin pair subsets, is indicated by large white circles (σ_1) and white triangles (σ_3) in each stereogram, respectively (see Yamaji & Sato, 2006). For these global-average stress solutions, the mean angular dispersion of the component subsets from the global average is given by the Mean Angular Stress Distance (MASD)-value (Yamaji & Sato, 2006).

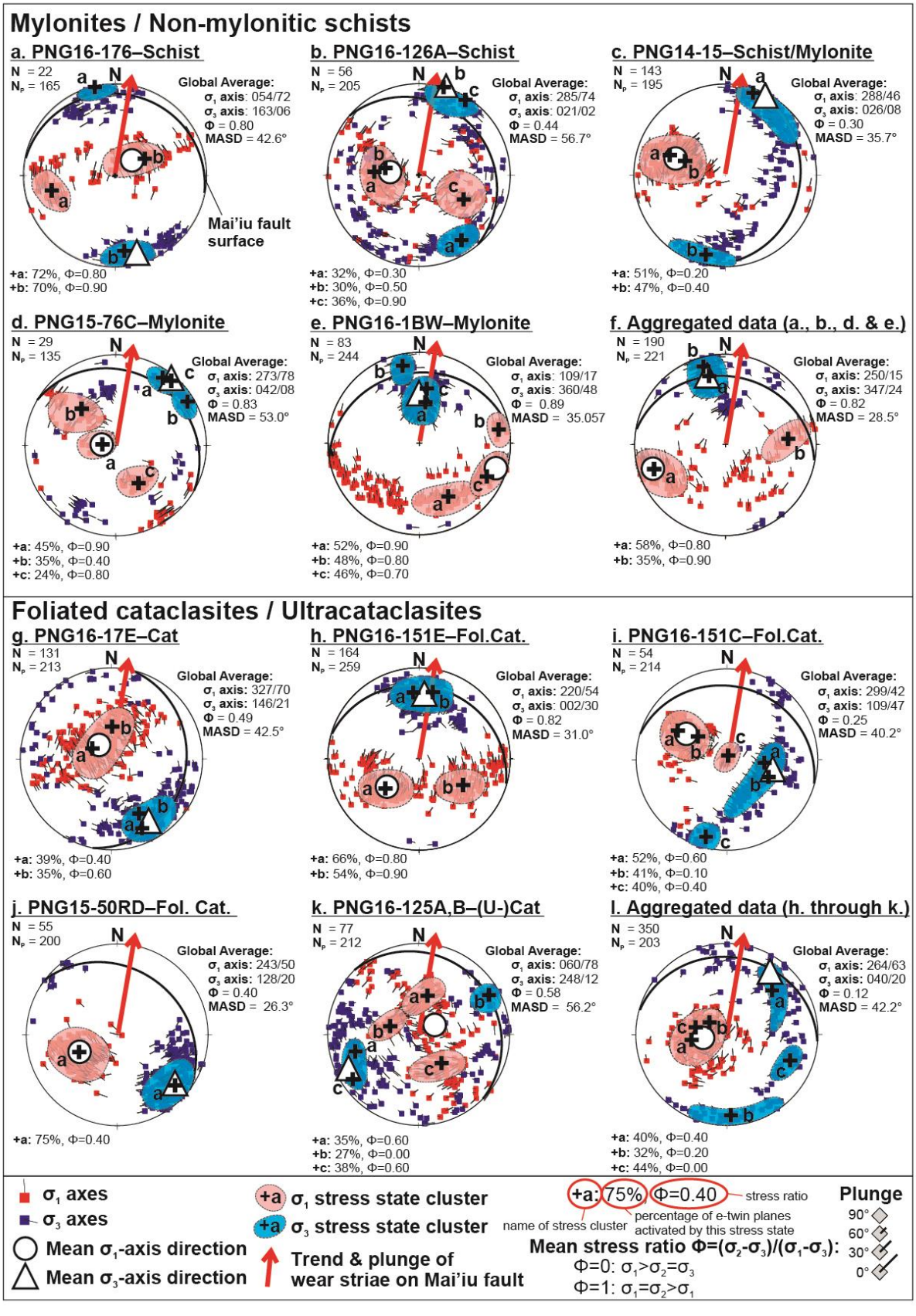
Mylonites / Non-mylonitic schists
a. PNG16-176–Schist
N = 22
Np = 165
Global Average:
σ1 axis: 054/72
σ3 axis: 163/06
Φ = 0.80
MASD = 42.6°
Mai'iu fault surface
+a: 72%, Φ=0.80
+b: 70%, Φ=0.90
b. PNG16-126A–Schist
N = 56
Np = 205
Global Average:
σ1 axis: 285/74
σ3 axis: 021/02
Φ = 0.44
MASD = 56.7°
+a: 32%, Φ=0.30
+b: 30%, Φ=0.50
+c: 36%, Φ=0.90
c. PNG14-15–Schist/Mylonite
N = 143
Np = 195
Global Average:
σ1 axis: 288/46
σ3 axis: 026/08
Φ = 0.30
MASD = 35.7°
+a: 51%, Φ=0.20
+b: 47%, Φ=0.40
d. PNG15-76C–Mylonite
N = 29
Np = 135
Global Average:
σ1 axis: 273/78
σ3 axis: 042/08
Φ = 0.83
MASD = 53.0°
+a: 45%, Φ=0.90
+b: 35%, Φ=0.40
+c: 24%, Φ=0.80
e. PNG16-1BW–Mylonite
N = 83
Np = 244
Global Average:
σ1 axis: 109/17
σ3 axis: 360/48
Φ = 0.89
MASD = 35.057
+a: 52%, Φ=0.90
+b: 48%, Φ=0.80
+c: 46%, Φ=0.70
f. Aggregated data (a., b., d. & e.)
N = 190
Np = 221
Global Average:
σ1 axis: 250/15
σ3 axis: 347/24
Φ = 0.82
MASD = 28.5°
+a: 58%, Φ=0.80
+b: 35%, Φ=0.90
Foliated cataclasites / Ultracataclasites
g. PNG16-17E–Cat
N = 131
Np = 213
Global Average:
σ1 axis: 327/70
σ3 axis: 146/21
Φ = 0.49
MASD = 42.5°
+a: 39%, Φ=0.40
+b: 35%, Φ=0.60
h. PNG16-151E–Fol.Cat.
N = 164
Np = 259
Global Average:
σ1 axis: 220/54
σ3 axis: 002/30
Φ = 0.82
MASD = 31.0°
+a: 66%, Φ=0.80
+b: 54%, Φ=0.90
i. PNG16-151C–Fol.Cat.
N = 54
Np = 214
Global Average:
σ1 axis: 299/42
σ3 axis: 109/47
Φ = 0.25
MASD = 40.2°
+a: 52%, Φ=0.60
+b: 41%, Φ=0.10
+c: 40%, Φ=0.40
j. PNG15-50RD–Fol. Cat.
N = 55
Np = 200
Global Average:
σ1 axis: 243/50
σ3 axis: 128/20
Φ = 0.40
MASD = 26.3°
+a: 75%, Φ=0.40
k. PNG16-125A,B–(U-)Cat
N = 77
Np = 212
Global Average:
σ1 axis: 060/78
σ3 axis: 248/12
Φ = 0.58
MASD = 56.2°
+a: 35%, Φ=0.60
+b: 27%, Φ=0.00
+c: 38%, Φ=0.60
l. Aggregated data (h. through k.)
N = 350
Np = 203
Global Average:
σ1 axis: 264/63
σ3 axis: 040/20
Φ = 0.12
MASD = 42.2°
+a: 40%, Φ=0.40
+b: 32%, Φ=0.20
+c: 44%, Φ=0.00
σ1 axes
σ3 axes
Mean σ1-axis direction
Mean σ3-axis direction
+a σ1 stress state cluster
+a σ3 stress state cluster
Trend & plunge of wear striae on Mai'iu fault
+a: 75% Φ=0.40
stress ratio
name of stress cluster
percentage of e-twin planes activated by this stress state
Mean stress ratio Φ=(σ2-σ3)/(σ1-σ3):
Φ=0: σ1>σ2=σ3
Φ=1: σ1=σ2>σ1
Plunge
90°
60°
30°
0°

Figure 5. Reconstructed principal stress directions (lower hemisphere, equal-area stereograms) based on observed calcite-twin pairs as analysed by the MIM-method. Solutions for σ_1 (red) and σ_3 (blue) are indicated by filled squares. Red and blue shaded regions identify dense clusters of stress axis directions (σ_1 and σ_3, respectively) that are labelled "a", "b" and "c". The white circles and triangles depict global average stress directions based on averaging of all the constituent data subsets. Black great circles—orientation of the Mai'iu fault surface at the respective sample location. MASD—mean angular stress distance (see text for explanation); N—Number of calcite-twin pairs; N_P—Number of stress states plotted. Sample locations are shown on Figure 1b. All samples are from the footwall close to the active fault trace except 5c and 5g, which are from the footwall close to the inactive trace of the fault. Note, that the aggregated data used in parts 5f and 5l exclude data from the inactive Mai'iu fault trace veins (5c, 5g), as the fault rocks and veins beneath it, have been tilted east by up to 16° as a result of the synformal deformation on the western limb of the rider block (Figure 1b). a) PNG16-176 (nonmylonitic mafic schist). b) PNG16-126A (nonmylonitic mafic schist). c) PNG14-15 (phyllitic mylonite/schist). d) PNG15-76C (mylonite). e) PNG16-1BW-B (mylonite). f) Stress states calculated for aggregated data from all calcite vein samples (except 5c) in the mylonites and underlying schists. g) PNG16-17E (cataclasite). h) PNG16-151E (foliated cataclasite; Figure 3c). i) PNG16-151C (foliated cataclasite). j) PNG15-50RD (foliated cataclasite). k) PNG16-125A, B (foliated cataclasite/ultracataclasite). l) Stress states calculated for aggregated data from all calcite vein samples (except 5g) in the foliated cataclasites and ultracataclasites.

Based on this analysis, calcite veins in mylonites and nonmylonitic schists produce estimates for σ_1 that chiefly plunge subvertically or subhorizontally in an ~E–W direction (i.e., subparallel to the strike of the Mai'iu fault), and they yield estimated stress ratios (Φ) of ~0.30–0.89 (range of global averages). The corresponding σ_3 axes typically plunge subhorizontally in a ~N–S direction, which is subparallel to the direction of regional extension and to the slip vector on the Mai'iu fault, with some plunging slightly more shallowly or steeply to the N than the dip of the Mai'iu fault, and others (less commonly) trending gently to the south (Figures 5a–5e). Stress directions calculated from the aggregated dataset of all calcite veins in the mylonites and nonmylonitic schists (combining datasets a.–e. in Figure 5) are shown in Figure 5f. This compiled data yields an average solution for σ_1 that plunges gently WSW (250/15) and one for

σ_3 that plunges NW (347/24) together with a mean stress ratio (Φ) of 0.82, indicative of a constrictional stress state (i.e., $\sigma_1 \approx \sigma_2$).

Stress solutions derived from twin pairs in deformed calcite veins in the structurally overlying foliated cataclasites and ultracataclasites are more complex and variable. They mostly record σ_1 directions that populate subvertical clusters carrying stress ratios of 0.25–0.82 and σ_3 axes that plunge subhorizontally in ~N–S direction or at an moderate angle (~47°) towards the east (Figures 5g–5k). The aggregated dataset from the foliated cataclasites and ultracataclasites (combining datasets h.–k., Figure 5l) indicate an overall subvertical σ_1 direction (264/63); σ_3 directions are quite scattered lying on a NW-SE striking great circle with a shallow dip direction towards the NE (at 040/20). The global average estimated stress ratio is low (Φ of ~0.12; i.e., $\sigma_2 \approx \sigma_3$), with individual subset solutions that are quite variable.

4.2 Paleo-Principal Stress Orientations and Stress Ratios based on Fault-slip Data for Late Brittle Faults

We infer paleo-principal stress orientations based on fault-slip data measured on mesoscopic (slip <1.5 m) faults cutting the footwall of the Mai'iu fault near the base of the scarp, which is the most recently exhumed part of the fault surface. The analyzed fault assemblage is dominated by normal faults and strike-slip faults (both dextral and sinistral). From these, we derived stress solutions based on: 1) an amalgamation of most of the fault-slip data spanning localities at a strike length of ~6 km to the west and ~20 km to the east of Biniguni Falls (Figure 6a); and 2) another large fault-slip dataset (not included in part a) that was collected at our most densely studied, single field locality (Biniguni Falls, Figure 6b—for location see Figure 1d); 3) fault slip data collected in the synclinal rider block, ~26 km to the east of Biniguni Falls (east-tilted, inactive part of the Mai'iu fault, Figure 6c); 4) fault-slip data from Biniguni Falls locality (same as part b) but analysed after attempting to restore the data for southward backtilting of the footwall by 30° and 40° (inferred rolling hinge deformation, Figure 6d); and 5) fault-slip data in former hangingwall strata of the Gwoira Conglomerate exposed in the rider block (using present-day orientations, Figure 6e, and after an attempted back-rotation to horizontal of stratal dips, Figure 6f).

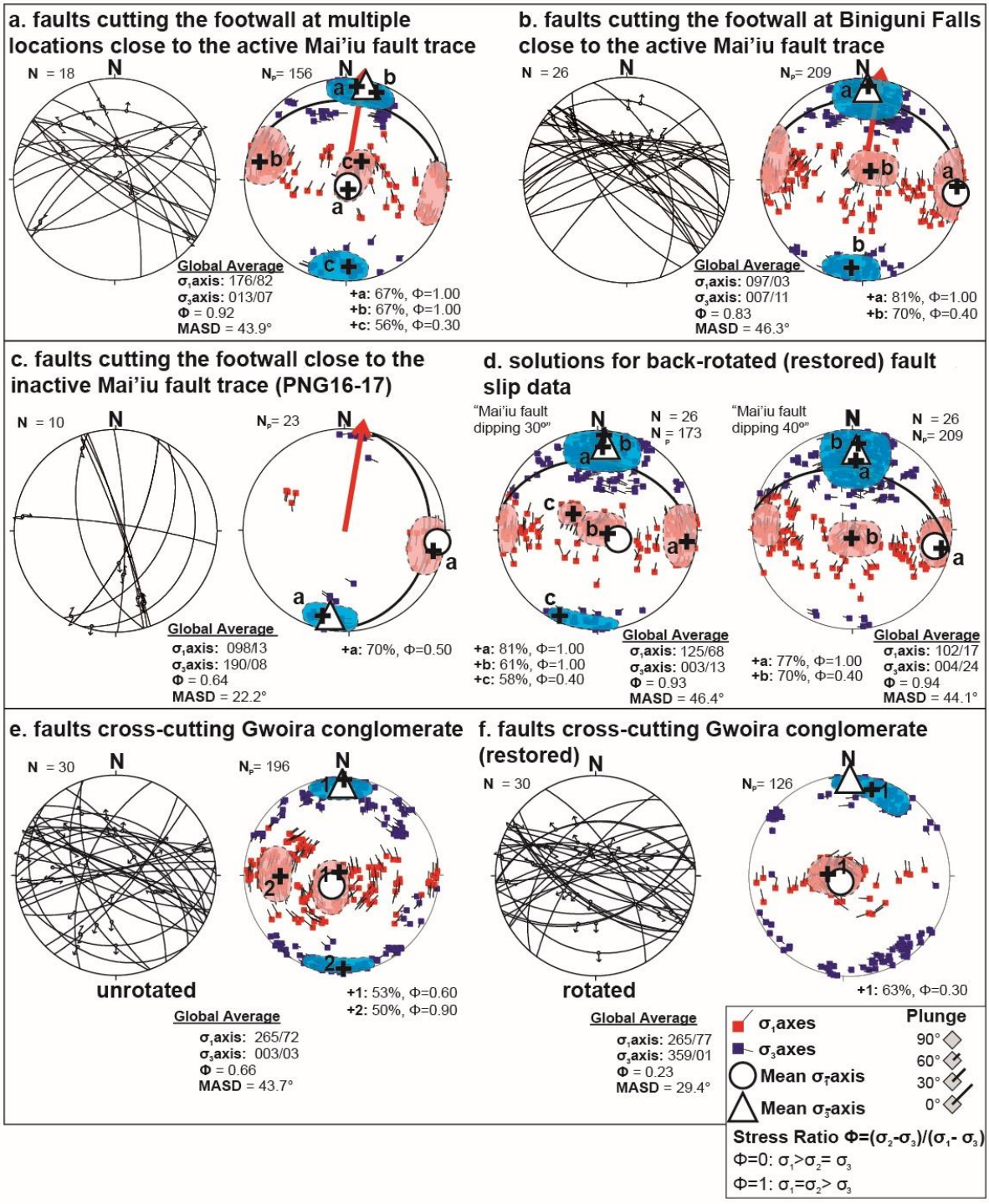

Figure 6. Fault-slip data and calculated paleo-principal stress axis solutions based on MIM analysis for small brittle faults cutting the northernmost footwall of the Mai'iu fault (e.g., Fig. 1f). a) Solutions based on all sites to the west and east of Biniguni Falls at sites PNG15-52, PNG15-76, PNG16-142, PNG15-50 and PNG16-151 (for locations, see Fig. 1b). b) Solutions based on Biniguni Falls location, PNG16-1BW (see Figs. 1b and 1d). c) Solutions based on data

562 collected beneath the abandoned and east-tilted part of the Mai'iu fault at site PNG16-17 (the
563 rider block, see Fig. 1b). d) Same as b., but stress inversion was undertaken after an initial
564 rotation of the fault-slip data about the local 103° strike of the Mai'iu fault to restore the Mai'iu
565 fault (now dipping 22° NE at the surface) to an inferred former dip of 30° (stereogram on left),
566 or of 40° (stereogram on right). e) Solutions based on present-day attitudes of the collected fault-
567 slip data (mostly steep normal faults) cutting the Pliocene strata (Gwoira Conglomerate, former
568 hangingwall of Mai'iu fault) in the rider block. f) Same as e., but, stress inversion was
569 undertaken after restoring the (generally southward) dip of bedding at each data locality to
570 horizontal by a rotation its strike. Heavy blue-colored great circles in parts a-d plot mean
571 attitude and striae plunge for the Mai'iu fault plane at each locality.
572
573 Based on our fault-slip data for small faults cutting the footwall along the active
574 rangefront, the calculated σ_1 axes fall into two main clusters:1) subvertical (Figure 6a); and 2)
575 plunging subhorizontally to the ENE or WNW; that is, subparallel to the strike of the Mai'iu
576 fault (Figure 6b). In both cases, mean solutions for σ_3 plunge subhorizontally to the NNE. The
577 mean stress ratios (Φ) range from 0.83 to 0.92, indicating that σ_1 and σ_2 are of subequal
578 magnitude ($\sigma_1 \approx \sigma_2$), corresponding to a constrictional stress state. These principal stress
579 orientations and stress ratios, based on fault-slip data, are similar to those inferred for calcite
580 veins in mylonites and nonmylonitic schists, based on the calcite twinning analysis (Figures 5a–
581 5f).
582 Farther east, in the rider block, mean solutions for σ_1 plunge subhorizontally to the ENE
583 whereas those for σ_3 plunge gently to the SSW (Figure 6c). The estimated stress ratio (Φ) is 0.64.
584 At this location, the Mai'iu fault is inactive and has been tilted ~16° east on the limb of a
585 syncline (Little et al., 2019). Attempting to back-restore the fault-slip data to account for this late
586 tilting does not result in a major change in the mean solutions for σ_1 and σ_3, except that σ_1 now
587 plunges gently towards the WNW.
588 The Ma'iu fault is known to have back-rotated (i.e., tilted southward to shallow its
589 northerly dip) as a result of a rolling-hinge unloading process (Mizera et al., 2019; Webber et al.,
590 2020; Watson et al., 2021). In an attempt to account for (remove) this late-stage tilting, we
591 rotated the fault slip data at Biniguni Falls (same data as used in Figure 6b) about the local strike
592 of the Mai'iu fault (103°) before inverting the data for best-fit stress orientations. This was done

in two different ways (Figure 6d): 1) by assuming that the Mai'iu fault (which today dips ~22° NNE at the surface at this locality) originally dipped 30° (left-hand stereogram) at the time when the small-scale faults formed; and 2) by assuming that it originally dipped 40° (right-hand stereogram). Regardless of the particular rotation used, the structurally restored fault-slip data yields mean solutions for σ_3 that plunge N or NNE at an angle that is 11° to 17° more shallow than the Mai'iu fault plane. With increasing inferred original dip of the Mai'iu fault at the time of brittle fault formation (transition from Figures 6b to 6d), the reconstructed plunge of σ_3 increases correspondingly (while still plunging slightly more shallowly than the fault). In all cases, mean σ_1 either plunges subhorizontally to the WNW or ENE—or it is subvertical (Figures 6b and 6d). Such "flipping" of σ_1 between subhorizontal and subvertical is not unexpected given the high stress ratios of Φ=0.83–0.94 ($\sigma_1 \approx \sigma_2$).

As a final exercise, we inverted fault-slip data in the former hangingwall of the Mai'iu fault (southwardly back-tilted strata of the Gwoira Conglomerate in the rider block) for best-fit stress directions. The analysed small-offset faults are almost entirely normal faults dipping at a moderate to steep angle relative to bedding. These include a mixture of both synthetic (down-to-the-north) and antithetic senses of slip. Inversion of these fault-slip data using their present-day orientations yields estimates for σ_1 that vary between subvertical to subhorizontal, (E-W trending, Figure 6e). The corresponding σ_3 axes plunge gently to the north or south. The global average of this dataset yields a subvertical σ_1, a N-trending, subhorizontal σ_3 and a stress ratio of Φ=0.66 (MASD=44°) and is thus almost "ideally" Andersonian. Despite a diversity of measured bedding and fault dips in the dataset, local bedding-fault angles everywhere remain 55–78°—a relationship that suggests that faulting predated most of the stratal tilting. To account for this, we first rotated every fault-slip datum about the local strike of bedding to restore that bedding to horizontal, before undertaking the stress analysis (Figure 6f). Such "unrotation" of the fault-slip data results in stress solutions that are less scattered and more homogenous (mean angular stress distance reduced from 44° to 29°). These solutions yield a mean trend of σ_3 that is NNE (rather than NS)—a result that accords better with the known extension direction of the Mai'iu fault and Woodlark rift.

4.3 Calcite Clumped Isotope Paleotemperatures

Clumped isotope analyses of calcite, including "conventional" oxygen and carbon isotope analyses, were performed to determine the temperature of calcite precipitation in veins and rock matrices and cements across the Mai'iu fault plane. The measured oxygen and carbon isotope ratios and their interpretation regarding the sources of the calcite-precipitating fluids are detailed in the Supporting Information S6. Clumped isotope thermometry of calcite in most samples of nonmylonitic schists and mylonites (n=7) yielded temperatures of 150–200°C (Supporting Information Table S6). These temperatures are well below inferred peak metamorphic temperatures of the Goropu Metabasalt (425±50°C; Daczko et al., 2009) and mostly below the temperature range estimated from calcite twin morphologies for calcite veins in the nonmylonitic schists and mylonites (>200–300°C and 250–400°C, respectively; see above). Thus, apart from perhaps the highest clumped isotope-based paleotemperatures—236±41°C and 223±12°C (for mylonite sample PNG15-52A)—the clumped isotope-based paleotemperatures for calcite veins in schist and mylonite samples do not document the crystallization temperatures of calcite. Rather, these probably represent blocking of isotope reordering in calcite during later exhumational cooling of the footwall, as has been shown for calcite marbles in other metamorphic core complexes (e.g., Stolper & Eiler, 2015; Ryb et al., 2017).

By contrast, calcite veins in the foliated cataclasites and ultracataclasites (n= 4) yield temperatures estimates ranging from 130±8°C to 160±14°C, mostly below calcite blocking temperatures, and thus may record original temperatures of calcite precipitation or recrystallization. Significant dynamic recrystallization of calcite veins in cataclasite sample PNG15-151 is indicated by EBSD imaging (Figures 3d and 3e). Recrystallization textures are observed primarily in older and more deformed, forward-inclined veins; these record mean paleotemperatures of ~160°C, whereas younger, thinner (and less deformed) foliation-perpendicular veins record a mean paleo-temperature of ~130° (Supporting Information Table S6). This temperature range (160-130°C) may bracket the interval between the minimum temperature of dynamic recrystallization of calcite (Ryb et al., 2017) and complete cessation of internal deformation of the cataclasites. Clumped isotope analyses of calcite cement (n=2) in the Gwoira Conglomerate of the hangingwall (sample PNG16-99, Figure 1b) yielded formation temperatures of 30±11°C and 32±12°C consistent with shallow burial of the conglomerate at the time of cementation.

5 Discussion

5.1 Disposition of Principal Stress Axes

Solutions for paleo-principal stress axes based on 1) twinning of calcite veins in footwall mylonites and adjacent nonmylonitic schists (Figures 5a–5f), and 2) on attitudes of small-offset brittle faults cutting the exhumed footwall (mylonites and cataclasites) of the Mai'iu fault (Figures 6a–6d) similarly indicate a stress state in which $\sigma_1 \approx \sigma_2 > \sigma_3$ ($\Phi \approx 0.64–0.94$; constrictional state of stress), and for which σ_3 plunges subhorizontally to the ~NNE or SSW (i.e., subparallel to the regional extension direction). In these solutions, σ_1 either plunges subhorizontally to the ESE or WNW (subparallel to the strike of the Mai'iu fault), or is subvertical (classic Andersonian extensional state of stress). Such apparent "flipping" of σ_1 in an otherwise Andersonian extensional stress state agrees with several previous field studies near ancient detachment faults that similarly inferred that σ_1 was either subvertical or arranged at a high angle (55°–80°) to the low-angle detachmant fault (e.g., Axen & Selverstone, 1994; Hayman et al., 2003; Axen, 2004, and references therein). In these cited studies, principal stress orientations were inferred from the attitude of mixed-mode extensional and shear fractures in the footwall and/or hangingwall of the detachment.

In the footwall of a major detachment fault, a constrictional state of stress ($\sigma_1 \approx \sigma_2$) may reflect reduction of subvertical stresses (caused by tectonic denudation from extensional fault slip and/or thinning of the hangingwall) coupled with an increase in strike-parallel horizontal stress during that denudation. The latter might be attributed to bending stresses in the extracted footwall, which is back-flexed during its exhumation (Fletcher et al., 1995; Singleton, 2013). During rolling-hinge-style flexural unbending of an exhumed footwall, the outer surface of this footwall contracts in the dip direction. At the same time, the footwall stretches and thickens at right angles to this. If the footwall is laterally confined parallel to fault strike (i.e., it is restricted by surrounding rocks), then the footwall cannot expand in this direction. This may lead to a syn-exhumational increase in strike-parallel compressive stress during fault slip, and thus to an increase in σ_2 magnitude. Such a constrictional state of stress might explain the common observation of extension-perpendicular shortening (and associated folding) as documented in the Buckskin-Rawhide MCC, west central Arizona, (e.g., Singleton, 2013); and indeed along the Mai'iu fault, where slip-parallel megacorrugations have been amplified in the near-surface as

682 active folds (Figures 7a and 7b; Little et al., 2019; Mizera et al., 2019). This model might explain
683 the high Φ-ratio ($\sigma_1 \approx \sigma_2$) and locally ~E–W trending σ_1 direction that we measured in the
684 footwall of the Mai'iu fault (Figures 5a–5f and 6a–6d).
685

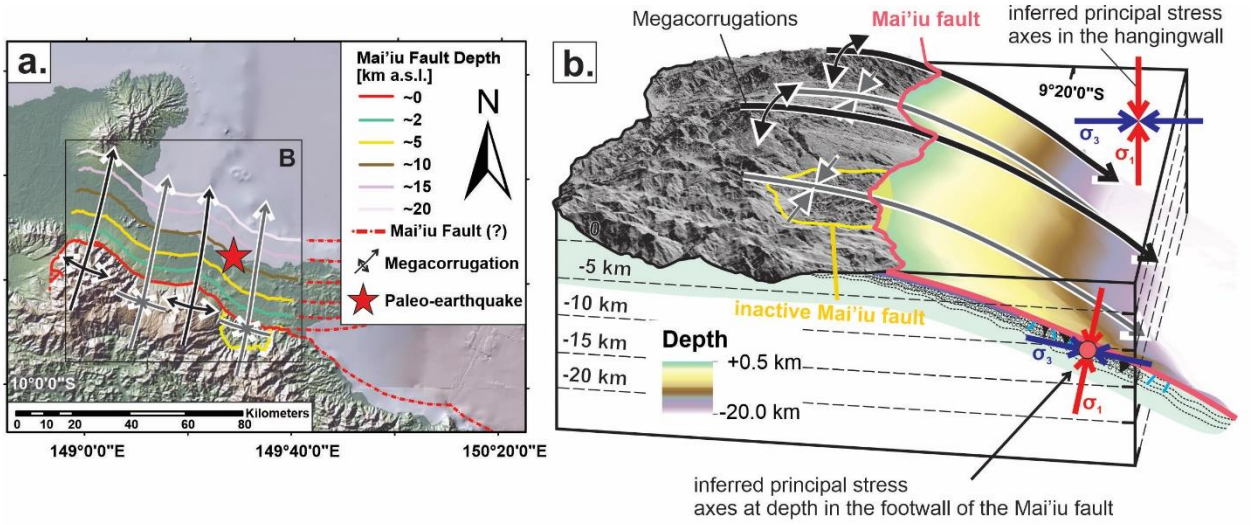

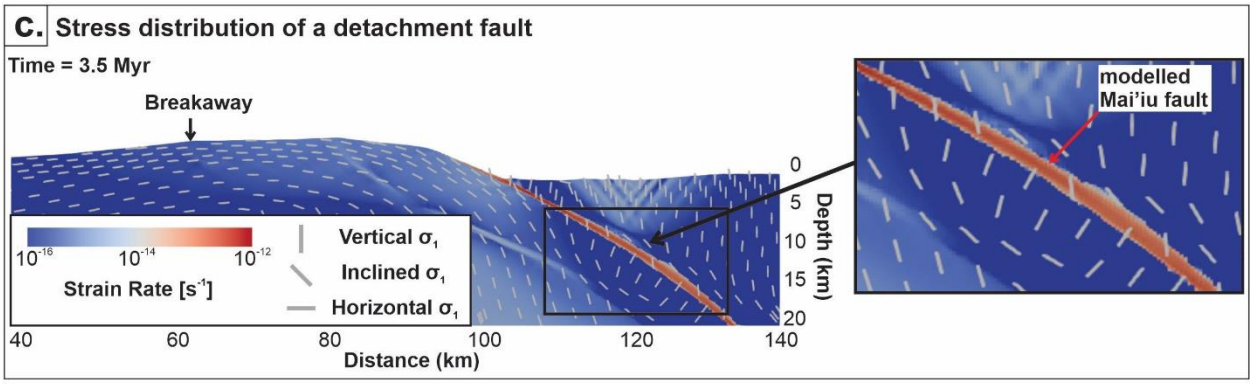

686

687 **Figure 7.** Inferred principal stress directions near the Mai'iu fault. a) Landsat image (30 m cell
688 size) draped over Shuttle Radar Topography Mission digital elevation model (~30 m cell size)
689 showing the Suckling-Dayman Metamorphic Core Complex (SDMCC) and megacorrugations
690 (black arrows). Red line—trace of the Mai'iu fault; yellow line—trace of the inactive Mai'iu
691 fault; coloured lines—inferred subsurface continuation of the Mai'iu fault after Abers et al.
692 (2016); red star—inferred formational depth of pseudotachylite veins (based on $^{40}Ar/^{39}Ar$ ages
693 from Little et al., 2019). b) Perspective view illustrating the corrugated fault surface of the
694 Mai'iu fault and its subsurface continuation. Principal stress axes σ_1 (red arrows) and σ_3 (blue
695 arrows) are based on Figure 6d (footwall) and Figure 6f (hangingwall). The red dot in the middle
696 of the footwall stress axes indicates that σ_1 and σ_2 are there of subequal magnitude (bending

697 stresses). c) Thermomechanical model from Biemiller et al. (2019) using boundary conditions
698 and rheological parameters tuned to the SDMCC. White glyphs—σ_1-orientations (see text).
699
700 The Mai'iu fault dips ~22±2° NNE at the surface (Figure 1b, inset). Most of our fault-slip
701 data-based solutions for the orientation of σ_3 either trend to the NNE and are subhorizontal; or
702 they plunge NNE or N at an angle that is less steep than the Mai'iu fault by 10–20°. Most
703 commonly, σ_1 is subvertical (Figures 6a–6d, 7b). Poles to calcite extension gashes can be
704 interpreted as recording the σ_3 direction. Except where they have been later strongly sheared,
705 these are mostly disposed at an angle of ~18–22° to the Mai'iu fault surface (Figure 1b, inset).
706 Such Andersonian to "near-Andersonian" (i.e., slightly inclined) stress directions are
707 unfavourable for slip on the shallow-dipping (at the surface) Mai'iu fault. If the apparent non-
708 zero plunge of σ_3 is real (i.e., Figure 6d) then the stresses were not exactly Andersonian, and σ_3
709 was at a small angle to the slip direction, a situation that would make slip on the fault even more
710 mechanically unfavourable than for an exactly Andersonian stress disposition. Such stress
711 obliquity is also implied by some of our calcite-twinning based solutions for stress orientation
712 (i.e., Figures 5e and 5h). A possible cause for local departures from Andersonian stress
713 orientation might be stress concentrations around geometric irregularities or asperities in the fault
714 zone (Chester & Fletcher, 1997; Chester & Chester, 2000; Rutter et al., 2007); however, near the
715 Mai'iu fault the pattern seems to be manifested across our entire dataset.
716 Figure 7c shows stress trajectories calculated as part of a geodynamic model exploring
717 reactivation of subduction thrusts as extensional detachments (see Mizera et al., 2019 and
718 Biemiller et al., 2019 for a detailed explanation of the model). This finite element model imposes
719 extensional velocity boundary conditions across a pre-weakened subduction zone, with the white
720 glyphs depicting trajectories of σ_1. The model reproduces a rolling-hinge evolution of the
721 detachment fault, with the exhumed portion becoming convex upward with continued extension.
722 The model is of interest here because it predicts spatial changes in stress orientation across the
723 Mai'iu fault. In the hangingwall of the fault, σ_1 is mostly vertical, but it deflects slightly
724 anticlockwise in proximity to the weak fault zone to become more nearly parallel to it. By
725 contrast, in the immediate footwall of the detachment, σ_1 deflects from the vertical in the
726 opposite sense to become more nearly perpendicular to the fault—with σ_3 arranged at a small
727 angle to the fault. At structurally higher footwall levels, adjacent to the fault, σ_1 deflects

anticlockwise to become more nearly Andersonian. In the model, the above-mentioned stress refractions in the footwall of the model reflect flexural stresses there, and they depend on the relative strengths of the footwall, the fault zone and the hangingwall materials. To what extent bending stresses affected the observed orientation of stress axes in our study cannot be answered, and the uncertainties in the calculated stress orientations are large. Nonetheless, the general state of footwall stress that we infer ($\sigma_1 \approx \sigma_2$; σ_1 subvertical, and σ_3 subhorizontal or plunging to the north at a small angle to the fault) accord with the predictions of this mechanical model.

In the foliated cataclasite and ultracataclasite units of the footwall, our calculated stress ratios (Φ) and principal stress directions similarly indicate a mostly subvertical σ_1, but the corresponding σ_3 axes trend and plunge variably (Figures 5g–5l). The high differential stresses estimated from twin densities in some of these veins (Figure 4c), and the occurrence of pseudotachylites in these fault rocks (Figures 1g and 3a) suggest that the locally high inferred differential stresses and variable stress orientations may reflect heterogeneous dynamic stress conditions related to seismic-cycle stress reorientations (e.g., see Figure 4 in Di Toro et al., 2005; Mello et al., 2010). In addition, processes like fragmentation and clast rotation after vein emplacement, inelastic bending around irregularities and/or local stress concentrations around asperities may have caused a deformational dispersion of twin orientations in the brittle fault rocks (e.g., Rutter et al., 2007).

5.2 Calcite Vein Formation and Deformation Temperatures

We can assign approximate deformation temperatures to fault rocks using microstructural observations of deformed calcite veins contained within them (Figure 4b; Supporting Information Table S7). Calcite veins in the mylonites and subjacent nonmylonitic schists contain recrystallized grains and mostly Type III and Type IV e-twins, suggesting deformational temperatures of 200–400°C (Burkhard, 1993). Calcite veins in the foliated cataclasites and ultracataclasites contain mostly Type II and Type I e-twins, suggesting deformation temperatures <200°C (Figure 4b). Previously published chlorite geothermometry data in mylonites and foliated cataclasites provide further constraints on emplacement temperature of the analysed calcite vein samples in this study (potentially deformation temperatures; Supporting Information Table S7; see also Mizera et al., 2020). The latter emplacement temperature estimates are based on the composition of chlorite grains occupying syntectonic microstructural sites, or less

758 deformed veins cross-cutting such microstructures. Based on these results, the emplacement and
759 inferred deformation temperatures of these calcite veins are bracketed to 150–350°C.
760 The estimated apparent formation temperatures of calcite veins in mylonites and
761 nonmylonitic schists obtained from clumped-isotope geothermometry (~150–200°C) are
762 consistently lower by 50–100°C than those based on either the microstructural observations or
763 the chlorite-based paleotemperatures for corresponding rocks (Supporting Information Table S7).
764 We infer that the clumped-isotope temperatures do not record the temperature at which calcite
765 precipitated in the veins, but the temperature at which isotope reordering was blocked during
766 later cooling of the exhuming footwall (Passey & Henkes, 2012; Stolper & Eiler, 2015).
767 Furthermore, dynamic recrystallization can reset the Δ_{47} values of calcite due to efficient
768 mobilization of carbonate ion-groups during dislocation glide along crystallographic planes (Ryb
769 et al., 2017). Consequently, we interpret the clumped-isotope geothermometer-estimated
770 temperatures of (recrystallized) calcite veins in the mylonites and schists as providing a
771 minimum temperature of dynamic recrystallization (Ryb et al., 2017). In the structurally higher
772 foliated cataclasites and ultracataclasites, the clumped-isotope geothermometer is preferred
773 because chlorite-based temperatures in these rocks are inadequate due to a preferred growth of
774 corrensite (mixed layer chlorite and saponite) instead of chlorite at low temperatures (e.g.,
775 Bevins et al., 1991), and because e-twin based deformation temperatures are imprecise.
776 In summary, we used a combination of different geothermometers to bracket
777 temperatures at which calcite precipitated and deformed in the suite of fault rocks. All
778 geothermometers and paleopiezometers applied in this study show a similar trend of increasing
779 temperature and decreasing stress with increasing formational depth of the fault rock unit
780 (Supporting Information S7). In summary, (a) calcite veins in mylonite and nonmylonitic schist
781 experienced differential stresses of ~28–135 MPa at temperatures ~200–400°C, and (b) calcite
782 veins in foliated cataclasites and ultracataclasites experienced differential stresses of ~68–185
783 MPa at temperatures 130–250°C. To assign these temperature constraints to a relevant depth on
784 the Mai'iu fault requires knowledge of the variation in local geothermal gradient near that
785 structure. The local geothermal gradient has been estimated to be as high as ~24°C/km (average
786 22 ±2°/km) in the upper 10 km, decreasing to ~14–16°C/km at >20 km depth based on a
787 combination of fault-proximal geological and thermochronological data (Daczko et al., 2009;
788 Österle, 2019; Little et al., 2019; Mizera et al., 2020), far-field drillhole temperatures and

789 regional heat flow data for the Woodlark Rift (Tjhin, 1976; Martinez et al., 2001), and
790 thermomechanical modelling of the fault at the relevant slip rate (Biemiller et al., 2019, 2020)
791 (see Supporting Information S8).

792 **5.3 Strength-Depth Profile of the Mai'iu fault**

793 Figure 8a is a schematic profile across the Suckling-Dayman Metamorphic Core
794 Complex showing inferred formational depths of key fault rock units in the footwall of the
795 Mai'iu fault and associated temperatures (Little et al., 2019; Mizera et al., 2020). The depicted
796 dip of the Mai'iu fault at the ground surface (21°) is that seen in outcrop along the profile in
797 Figure 1c (Mizera et al., 2019). Dip angles in the subsurface are constrained by microseismicity
798 foci at ~12–25 km depth that are colinear with the trace of the Mai'iu fault (based on a projection
799 of the microseismicity data ~40 km farther east of this profile as located by Abers et al., 2016).
800 The inferred depth at which the dated pseudotachylite veins formed (~9–16 km depth; Little et
801 al., 2019) is indicated by a red star.

802

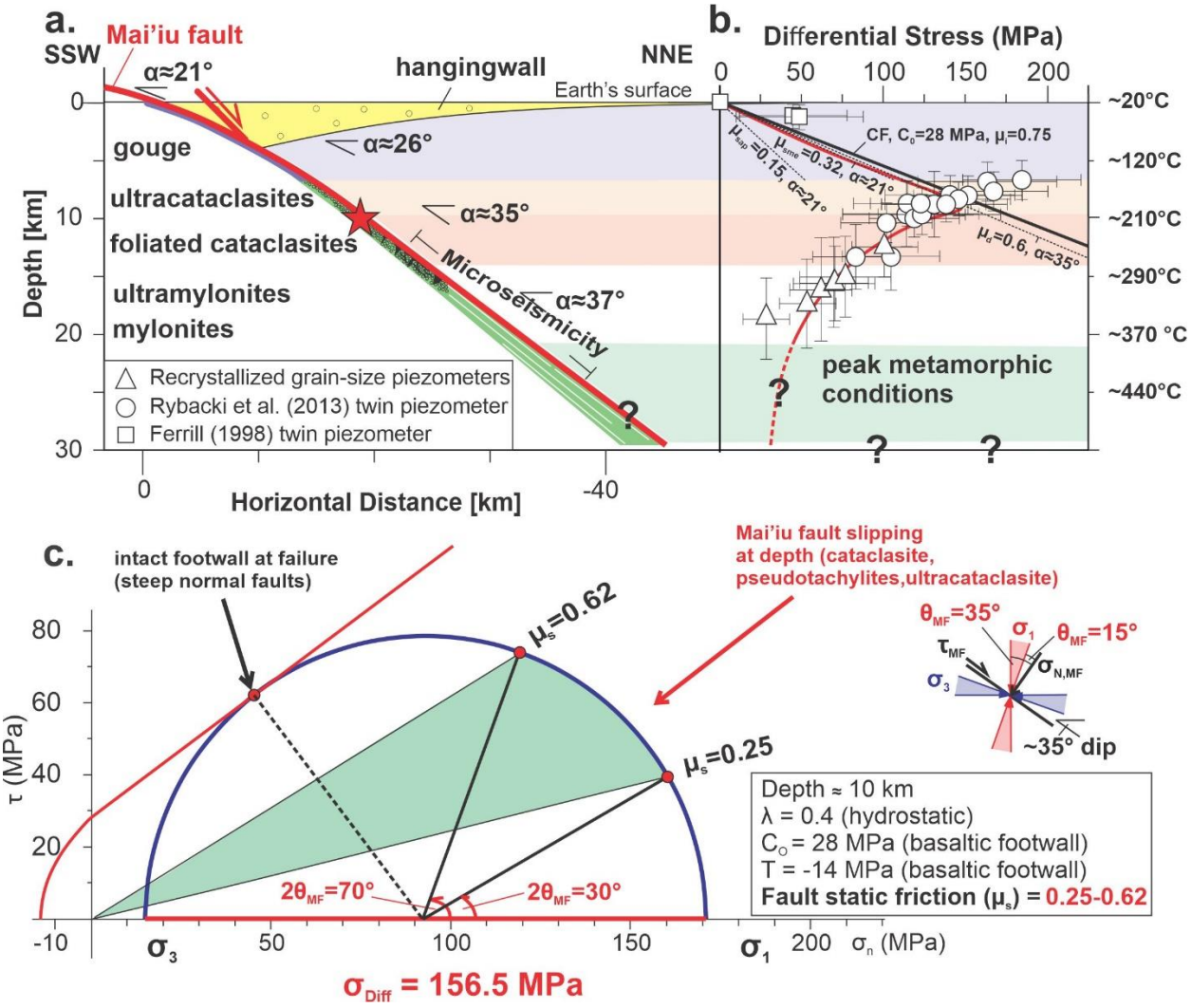

803

804 **Figure 8.** a) Depth profile of the Mai'iu fault (modified after Little et al., 2019; Mizera et al.,
805 2019). Microseismicity based on Abers et al. (2016). α—dip angle of the Mai'iu fault; Red
806 Star—formational depth of dated pseudotachylite veins. b) Differential stress versus depth-
807 temperature profile based on this study (Figure 4). The temperature-depth relationship used here
808 is outlined in Supporting Information S8 (inferred non-steady state geothermal structure). Brittle
809 failure curves for intact basaltic crust for which a linear Coulomb criteria (CF) limits differential
810 stress (this assumes a footwall cohesion, C_0, of 28 MPa, Schultz, 1993; and coefficient of
811 friction, μ_i, of 0.75). The lines through the origin depict a non-optimally oriented, cohesionless
812 fault with varying dip angles (α) and coefficient of frictions, for which reshear criteria limits
813 differential stress ($\mu_{sap,sme,d}$=0.15–0.6; dip angle of the fault, α=21–35°). μ_{sap}—coefficient of
814 friction for saponite (e.g., Lockner et al., 2011); μ_{sme}—coefficient of friction for smectite (e.g.,

Morrow et al., 2017); μ_d—"Byerlee" friction (Byerlee, 1978); red line—inferred change in strength of the Mai'iu fault with depth and temperature. c) Mohr circle depicting state of stress at 10 km depth near the Mai'iu fault. Assumes a static friction in the footwall (μ_S) of 0.75 and hydrostatic pore fluid pressure ratio of (λ=0.4) under variably Andersonian (vertical σ_1) to slightly non-Andersonian stress (σ_1 plunging steeply south at 70°) regime (based on calcite veins and late brittle faults in the footwall of the Mai'iu fault). To allow reshearing on the misoriented Mai'iu fault (here dipping 35°, see part a), the coefficient of sliding friction on the fault (μ_s) must be less than 0.6 (bottom end of "Byerlee" friction; Byerlee, 1978). For reference, a failure line for μ_s = 0.24 is also shown (corresponding to a smectite-rich gouge; e.g., Biemiller et al., 2020). Note that even for μ_s = 0.6, a differential stress of ~157 MPa would drive both reshear on the Mai'iu fault and brittle yielding of its metabasaltic footwall.

In Figure 8b, we plot differential stresses versus depth based on our calcite paleopiezometric studies (Figures 4a, 4c), and the estimated deformation temperatures of the calcite veins (Figure 4b; Supporting Information S6 and S7), with these temperatures being converted to depths using an estimate of the thermal structure that is presented in Supporting Information S8 (including Figure S8). The error bars on each differential stress data point accommodate: a) the standard deviation (1σ) of the mean twin density in the analysed calcite grains (Figure 4c); b) the deviation between the Valcke et al. (2015) and Platt and De Bresser (2017) recrystallized grain-size paleopiezometer (Figure 4a); c) the uncertainties in deformation temperatures (vertical bars; Supporting Information Table S7); and d) the uncertainties in geothermal gradient (Supporting Information S8). In Figure 8b several brittle failure curves are depicted in the strength-depth profile assuming Andersonian stresses (σ_1 is vertical) and a hydrostatic pore fluid pressure ratio (λ=0.4). The thick black failure curve represents failure of intact basaltic crust for which a linear Coulomb Failure criteria (CF) limits differential stress (cohesion, C_0=28 MPa, Schultz, 1993; coefficient of friction, μ_i=0.75), and in which faults are ideally oriented. The several dotted curves represent reshear conditions for non-optimally oriented, cohesionless faults at dips (α) of 21° or 35°; and at static coefficients of friction (μ_d) of 0.15, 0.32, or 0.6. The equations for the brittle failure curves and material parameters used in this plot are presented in Supporting Information S10.

According to this profile (Figure 8b), calcite veins in the mylonites formed at depths of 20–12 km depth, and experienced differential stresses of 25–135 MPa, with the average stress magnitude increasing with decreased temperature and depth. A peak in differential stress at ~6–12 km depth was measured in calcite veins from the foliated cataclasites, which hosts ultracataclasite bands and pseudotachylite veins. There, we measured some differential stresses >150 MPa—a value that exceeds the theoretical brittle strength curve for intact basaltic rocks (CF). This is in accordance with our observation that newly formed brittle faults cut the metabasaltic footwall of the Mai'iu fault (e.g., Figures 1f and 1g). Despite this localized yielding in the footwall, the Mai'iu fault as a whole remains viable—and its continued slip eventually led to exhumation of its (mesoscopically faulted) footwall. Given the large differential stresses near the stress peak at ~6–12 km depth, such reshear would have been possible for any coefficient of friction <0.6 if the mean dip of the fault at this depth is ~35° (Figure 8b).

At shallower depths of <6 km, where the fault dips ~21°, the fault strength is controlled by the frictional properties of the clay-rich fault gouge. Abundant saponite and corrensite were identified in Mai'iu fault gouges by XRD-analysis on parts of the fault, both active and inactive, that dip <21° (sites PNG16-142 and PNG16-17, Little et al., 2019; Mizera et al., 2020; Biemiller et al., 2020). We infer from the known stability range of saponite (T<~150°C; e.g., Lockner et al., 2011), that the saponitic gouges formed at shallow depths (<6 km) by pervasive alteration of the mafic footwall (Mizera et al., 2020), thus forming a frictionally weak rock that is also prone to aseismic creep (velocity-strengthening behaviour; Biemiller et al., 2020). There, we consider reshear criteria appropriate to a saturated saponite- or smectite-rich fault gouge (μ_{sap}≈0.15, μ_{sme}≈0.32; Lockner et al., 2011; Morrow et al., 2017; Biemiller et al., 2020). Figure 8b shows that the differential stresses required for the fault to slip at this shallower and more misoriented dip angle depend on the fault friction coefficient. The maximum allowable friction coefficient on the Mai'iu fault would be that corresponding to a differential stress (for reshearing) that is equal in magnitude to that required for intact fracture of the footwall by ideally oriented faults (CF failure line). For a Mai'iu fault dip of 21°, this friction coefficient is ~0.38. For an active fault dip that is locally as low as 16° the maximum allowable coefficient of friction would be ~0.28, coincident with the maximum coefficient of friction reported for Mai'iu fault saponite-rich gouges (Biemiller et al., 2020). We note that the brittle failure curves presented here assume

Andersonian stresses; however, our results suggest that the principal stress axes may not be strictly Andersonian in the footwall of the Mai'iu fault (see above).

5.4 State of Stress at Depth on the Mai'iu Fault

Twinning-based differential stress estimates in the foliated cataclasites and ultracataclasites (140–185 MPa; which formed at temperatures ~130–275°C, Mizera et al., 2020) are interpreted to record those present at our inferred mid-crustal differential stress peak at 6–12 km depth (Little et al., 2019). The degree to which these stress estimates may reflect interseismic stresses rather than short-lived, dynamic ones during earthquakes is uncertain. Pseudotachylite veins injected into the foliated cataclasites (Figures 1g and 3a), and solutions for stress orientations in those rocks that are complex and heterogeneous (Figures 5g–5k) suggest that at least some of our differential stress estimates—presumably the highest ones—may reflect dynamic stresses during the earthquake cycle. We have estimated a mean differential stress (σ_{Diff}) for the foliated cataclasites and ultracataclasites of ~157±36 MPa (Figure 4c). Assuming that this mean value is representative of the long-term, interseismic peak strength on the Mai'iu fault at ~10 km depth, we can construct a Mohr circle diagram to depict this situation (Figure 8c). To do so, we allow σ_1 to range between vertical (ideal Andersonian stress state, σ_1 at a 55° angle to the 35°-dipping fault) to slightly inclined (i.e., non-Andersonian, with σ_1 disposed at ~75° to the 35°-dipping fault). We note that calcite veins in the fault rocks may indicate fluid pressures sufficiently high at times to induce local hydrofracturing (i.e., $P_f > \sigma_3$); however, fluid influx was not high enough to completely retrogress the metabasaltic mineral assemblage as observed in other MCCs such as the Moresby Seamount Detachment in the eastern Woodlark Rift (cf. Speckbacher et al., 2012, 2013). Overall, there is little evidence for sustained fluid flow or high pore fluid pressure in the foliated cataclasites, which contains ductilely sheared calcite veins (e.g., Figures 3b and 3c; Mizera et al., 2020). Thus, we assign pore fluid pressure ratio of λ=0.4 (hydrostatic). Assuming a 35° dipping Mai'iu fault in the subsurface, our paleo-differential stress measurements indicate that to drive slip on such a fault the mean coefficient of static friction must have been ~0.25–0.62 in the foliated cataclasites. At times, differential stresses must have been high enough (>150 MPa) to cause new brittle yielding of formerly intact, strong mafic footwall rocks, as is expressed by small faults cutting the exhumed fault surface (Figures 1f and 1g).

6 Conclusions

Our study documents differential stresses, principal stress orientations, and temperatures occurring near the active Mai'iu low-angle normal fault which has self-exhumed a sequence of fault rocks that formed as the footwall was carried up through the mid crust to the surface. We have applied paleostress and geothermometry analyses to the exhumed metabasaltic footwall rocks and to conglomerates in the Gwoira rider block (former hangingwall) to reconstruct a strength-profile through the middle crust in this region. Our results show that:

- Solutions for the orientation of σ_1 and high stress ratios (Φ) of >0.8 reflect σ_1 and σ_2 that were subequal in magnitude, with significant compression subparallel to the strike of the Mai'iu fault. We attribute this to a combination of vertical unloading as a result of finite dip-slip on the fault together with 3-D bending stresses related to rolling-hinge style flexure of the footwall.
- Differential stresses in the deepest formed mylonites and nonmylonitic schists in the footwall of the Mai'iu fault ranged from >25 MPa at ~18 km depth up to 135 MPa at ~12 km depth.
- In the foliated cataclasites and ultracataclasites, peak differential stresses reached ~140–185 MPa (mean 157±36 MPa) at 6–12 km depth. The high differential stresses and the heterogeneity of stress solutions in these fault rocks were found to coincide with the occurrence of pseudotachylite veins at this depth cross-cutting the foliated cataclasites; thus suggesting that at least some of our stress estimates may reflect dynamic stresses during the earthquake cycle.
- The differential stresses supported by the mid-crustal foliated cataclasites were at times high enough (>150 MPa) to cause new brittle yielding of strong, formerly intact mafic footwall rocks and to drive slip on a moderately dipping part of the Mai'iu fault that was relatively strong.
- At the shallowest crustal levels (<6 km; T<150°C), the Mai'iu fault is a true low-angle normal fault, dipping ~22±2°, and is highly misoriented. This situation is probably overcome by the fault having a relatively low effective coefficient of friction there (μ<0.38, saponite-rich gouge).

Acknowledgments, Samples, and Data

Marsden Fund grant VUW1310 provided financial support to conduct this research. We are grateful to Hugh Davies (University of Papua New Guinea) and Ian Smith (University of Auckland) for providing field book scans and discussions. We thank Susan Ellis, Samuel Webber, Jürgen Österle, Laura Wallace, Kevin Norton, and Daniel Stockli for field support and discussions. Special thanks go to the many landowners, oral chiefs, elders, and citizens who granted us permission to study their land. We also thank our guides and carriers without whom this work would not have been possible.

All structural data from the Suckling-Dayman Metamorphic Core Complex, raw EBSD data of analysed calcite veins and MATLAB codes used in this study can be obtained from the Data Repository (Mizera et al., 2021: http://dx.doi.org/10.17632/mkpgbs4hf3.1). Additional information on fault rocks analyzed in this study can be found in the research archive of Victoria University of Wellington (http://hdl.handle.net/10063/8666, Mizera, 2019).

References

Abers, G. A. (2009). Slip on shallow-dipping normal faults. Geology, 37(8), 767-768. https://doi.org/10.1130/focus082009.1.

Abers, G. A., Eilon, Z., Gaherty, J. B., Jin, G., Kim, Y. H., Obrebski, M., & Dieck, C. (2016). Southeast Papuan crustal tectonics: Imaging extension and buoyancy of an active rift. Journal of Geophysical Research: Solid Earth, 121(2), 951–971. https://doi.org/10.1002/2015jb012621

Anderson, E. M. (1951). The dynamics of faulting and dyke formation: with applications to Britain. Edinburgh and London: Oliver and Boyd.

Angelier, J. T., & Mechler, P. (1977). Sur une methode graphique de recherche des contraintes principales egalement utilisables en tectonique et en seismologie: la methode des diedres droits. Bulletin de la Société géologique de France, 7(6), 1309-1318.

Axen, G. J. (1992). Pore pressure, stress increase, and fault weakening in low-angle normal faulting. Journal of Geophysical Research: Solid Earth, 97(B6), 8979-8991. https://doi.org/10.1029/92JB00517

962 Axen, G. J., & Selverstone, J. (1994). Stress state and fluid-pressure level along the Whipple
963 detachment fault, California. Geology, 22(9), 835-838. https://doi.org/10.1130/0091-
964 7613(1994)022%3C0835:SSAFPL%3E2.3.CO;2
965 Axen, G. J., & Hartley, J. M. (1997). Field tests of rolling hinges: Existence, mechanical types,
966 and implications for extensional tectonics. Journal of Geophysical Research: Solid Earth,
967 102(B9), 20515–20537. https://doi.org/10.1029/97JB01355
968 Axen, G. J. (2004). Low-angle normal fault mechanics and crustal strength. In G. Karner (Ed.),
969 Rheology and deformation of the lithosphere (pp. 46–91). New York, NY: Columbia
970 University Press.
971 Axen, G. J. (2007). Research Focus: Significance of large-displacement, low-angle normal
972 faults. Geology, 35(3), 287–288. https://doi.org/10.1130/0091-
973 7613(2007)35[287:rfsoll]2.0.co;2
974 Barber, D. J., & Wenk, H. R. (1979). Deformation twinning in calcite, dolomite, and other
975 rhombohedral carbonates. Physics and Chemistry of Minerals, 5(2), 141-165.
976 https://doi.org/10.1007/BF00307550
977 Behr, W. M., & Platt, J. P. (2011). A naturally constrained stress profile through the middle crust
978 in an extensional terrane. Earth and Planetary Science Letters, 303(3-4), 181-192.
979 https://doi.org/10.1016/j.epsl.2010.11.044
980 Behr, W. M., & Platt, J. P. (2014). Brittle faults are weak, yet the ductile middle crust is strong:
981 Implications for lithospheric mechanics. Geophysical Research Letters, 41(22), 8067-
982 8075. https://doi.org/10.1002/2014GL061349
983 Bevins, R. E., Robinson, D., & Rowbotham, G. (1991). Compositional variations in mafic
984 phyllosilicates from regional low-grade metabasites and application of the chlorite
985 geothermometer. Journal of Metamorphic Geology, 9(6), 711–721.
986 https://doi.org/10.1111/j.1525-1314.1991.tb00560.x
987 Biemiller, J., Ellis, S., Mizera, M., Little, T., Wallace, L., & Lavier, L. (2019). Tectonic
988 inheritance following failed continental subduction: A model for core complex formation
989 in cold, strong lithosphere. Tectonics, 38(5), 1742–1763.
990 https://doi.org/10.1029/2018TC005383
991 Biemiller, J., Boulton, C., Wallace, L., Ellis, S., Little, T., Mizera, M., et al. (2020). Mechanical
992 implications of creep and partial coupling on the world's fastest slipping low-angle

993 normal fault in southeastern Papua New Guinea. Journal of Geophysical Research: Solid
994 Earth, 125(10). https://doi.org/10.1029/2020jb020117
995 Bonifacie, M., Calmels, D., Eiler, J. M., Horita, J., Chaduteau, C., Vasconcelos, C., ... &
996 Bourrand, J. J. (2017). Calibration of the dolomite clumped isotope thermometer from 25
997 to 350 C, and implications for a universal calibration for all (Ca, Mg, Fe) CO3
998 carbonates. Geochimica et Cosmochimica Acta, 200, 255-279.
999 https://doi.org/10.1016/j.gca.2016.11.028
1000 Bourdelle, F., & Cathelineau, M. (2015). Low-temperature chlorite geothermometry: A graphical
1001 representation based on a T–R2+–Si diagram. European Journal of Mineralogy, 27(5),
1002 617–626. https://doi.org/10.1127/ejm/2015/0027-2467
1003 Brand, W. A., Assonov, S. S., & Coplen, T. B. (2010). Correction for the 17O interference in δ
1004 (13C) measurements when analyzing CO2 with stable isotope mass spectrometry
1005 (IUPAC Technical Report). Pure and Applied Chemistry, 82(8), 1719-1733.
1006 https://doi.org/10.1351/PAC-REP-09-01-05
1007 Brandstätter, J., Kurz, W., & Rogowitz, A. (2017). Microstructural analysis and calcite
1008 piezometry on hydrothermal veins: Insights into the deformation history of the Cocos
1009 Plate at Site U1414 (IODP Expedition 344). Tectonics, 36(8), 1562-1579.
1010 https://doi.org/10.1002/2017TC004490
1011 Buck, W. R. (1990). Comment on "Origin of regional, rooted low-angle normal faults: A
1012 mechanical model and its tectonic implications" by An Yin. Tectonics, 9(3), 545–546.
1013 https://doi.org/10.1029/TC009i003p00545
1014 Burkhard, M. (1993). Calcite twins, their geometry, appearance and significance as stress-strain
1015 markers and indicators of tectonic regime: a review. Journal of structural geology, 15(3-
1016 5), 351-368. https://doi.org/10.1016/0191-8141(93)90132-T
1017 Byerlee, J. (1978). Friction of rocks. Pure and applied geophysics, 116(4-5), 615-626.
1018 Cathelineau, M. (1988). Cation site occupancy in chlorites and illites as function of temperature.
1019 Clay Minerals, 23(4), 471–485. https://doi.org/10.1180/claymin.1988.023.4.13
1020 Chester, J. S., & Fletcher, R. C. (1997). Stress distribution and failure in anisotropic rock near a
1021 bend on a weak fault. Journal of Geophysical Research: Solid Earth, 102(B1), 693-708.
1022 https://doi.org/10.1029/96JB02791

1023 Chester, F. M., & Chester, J. S. (2000). Stress and deformation along wavy frictional faults.
1024 Journal of Geophysical Research: Solid Earth, 105(B10), 23421-23430.
1025 https://doi.org/10.1029/2000JB900241
1026 Chiaraluce, L., Chiarabba, C., Collettini, C., Piccinini, D., & Cocco, M. (2007). Architecture and
1027 mechanics of an active low-angle normal fault: Alto Tiberina fault, Northern Apennines,
1028 Italy. Journal of Geophysical Research, 112(B10). https://doi.org/10.1029/2007JB005015
1029 Chiaraluce, L., Amato, A., Carannante, S., Castelli, V., Cattaneo, M., Cocco, M., & Marzorati, S.
1030 (2014). The Alto Tiberina near fault observatory (Northern Apennines, Italy). Annals of
1031 Geophysics, 57(3), 1–16. https://doi.org/10.4401/ag-6426
1032 Choi, E., & Buck, W. R. (2012). Constraints on the strength of faults from the geometry of rider
1033 blocks in continental and oceanic core complexes. Journal of Geophysical Research,
1034 117(B4). https://doi.org/10.1029/2011JB008741
1035 Collettini, C., & Sibson, R. H. (2001). Normal faults, normal friction? Geology, 29(10), 927–
1036 930. https://doi.org/10.1130/0091-7613(2001)029<0927:NFNF>2.0.CO;2
1037 Collettini, C., & Barchi, M. R. (2004). A comparison of structural data and seismic images for
1038 low-angle normal faults in the Northern Apennines (Central Italy): constraints on activity.
1039 Geological Society, London, Special Publications, 224(1), 95-112.
1040 https://doi.org/10.1144/GSL.SP.2004.224.01.07
1041 Collettini, C., Niemeijer, A., Viti, C., & Marone, C. (2009a). Fault zone fabric and fault
1042 weakness. Nature, 462(7275), 907–910. https://doi.org/10.1038/nature08585
1043 Collettini, C., Viti, C., Smith, S. A., & Holdsworth, R. E. (2009b). Development of
1044 interconnected talc networks and weakening of continental low-angle normal faults.
1045 Geology, 37(6), 567-570. https://doi.org/10.1130/G25645A.1
1046 Collettini, C. (2011). The mechanical paradox of low-angle normal faults: Current understanding
1047 and open questions. Tectonophysics, 510(3), 253–268.
1048 https://doi.org/10.1016/j.tecto.2011.07.015
1049 Cooper, F. J., Platt, J. P., & Behr, W. M. (2017). Rheological transitions in the middle crust:
1050 Insights from Cordilleran metamorphic core complexes. Solid Earth, 8(1), 199.
1051 https://doi.org/10.5194/se-8-199-2017

1052 Craddock, J. P., & Magloughlin, J. F. (2005). Calcite strains, kinematic indicators, and magnetic
1053 flow fabric of a Proterozoic pseudotachylyte swarm, Minnesota River valley, USA.
1054 Tectonophysics, 402(1-4), 153-168. https://doi.org/10.1016/j.tecto.2004.12.035
1055 Cross, A. J., Prior, D. J., Stipp, M., & Kidder, S. (2017). The recrystallized grain size piezometer
1056 for quartz: An EBSD-based calibration. Geophysical Research Letters, 44(13), 6667-
1057 6674. https://doi.org/10.1002/2017GL073836
1058 Daczko, N. R., Caffi, P., Halpin, J. A., & Mann, P. (2009). Exhumation of the Dayman dome
1059 metamorphic core complex, eastern Papua New Guinea. Journal of Metamorphic
1060 Geology, 27(6), 405–422. https://doi.org/10.1111/j.1525-1314.2009.00825.x
1061 Daczko, N. R., Caffi, P., & Mann, P. (2011). Structural evolution of the Dayman dome
1062 metamorphic core complex, eastern Papua New Guinea. Bulletin, 123(11–12), 2335–
1063 2351. https://doi.org/10.1130/B30326.1
1064 Davies, H. L. (1978). Folded thrust fault and associated metamorphism in the Suckling-Dayman
1065 massif, Papua New Guinea. Geological Survey of Papua New Guinea, 280-A, 171–191.
1066 De Bresser, J. H. P., & Spiers, C. J. (1997). Strength characteristics of the r, f, and c slip systems
1067 in calcite. Tectonophysics, 272(1), 1-23. https://doi.org/10.1016/S0040-1951(96)00273-9
1068 Dennis, K. J., & Schrag, D. P. (2010). Clumped isotope thermometry of carbonatites as an
1069 indicator of diagenetic alteration. Geochimica et Cosmochimica Acta, 74(14), 4110-4122.
1070 https://doi.org/10.1016/j.gca.2010.04.005
1071 Di Toro, G., Nielsen, S., & Pennacchioni, G. (2005). Earthquake rupture dynamics frozen in
1072 exhumed ancient faults. Nature, 436(7053), 1009. https://doi.org/10.1038/nature03910
1073 Eiler, J. M. (2011). Paleoclimate reconstruction using carbonate clumped isotope thermometry.
1074 Quaternary Science Reviews, 30(25-26), 3575-3588.
1075 https://doi.org/10.1016/j.quascirev.2011.09.001
1076 Engelder, T. (1979). Mechanisms for strain within the Upper Devonian clastic sequence of the
1077 Appalachian Plateau, western New York. American Journal of Science, 279(5), 527-542.
1078 https://doi.org/10.2475/ajs.279.5.527
1079 Evans, M. A., & Dunne, W. M. (1991). Strain factorization and partitioning in the North
1080 Mountain thrust sheet, central Appalachians, USA. Journal of Structural Geology, 13(1),
1081 21-35. https://doi.org/10.1016/0191-8141(91)90098-4

1082 Faulkner, D. R., Mitchell, T. M., Healy, D., & Heap, M. J. (2006). Slip on 'weak' faults by the
1083 rotation of regional stress in the fracture damage zone. Nature, 444(7121), 922.
1084 https://doi.org/10.1038/nature05353
1085 Ferrill, D. A. (1998). Critical re-evaluation of differential stress estimates from calcite twins in
1086 coarse-grained limestone. Tectonophysics, 285(1-2), 77-86.
1087 https://doi.org/10.1016/S0040-1951(97)00190-X
1088
1089 Ferrill, D. A., Morris, A. P., Evans, M. A., Burkhard, M., Groshong Jr, R. H., & Onasch, C. M.
1090 (2004). Calcite twin morphology: a low-temperature deformation geothermometer.
1091 Journal of structural Geology, 26(8), 1521-1529.
1092 https://doi.org/10.1016/j.jsg.2003.11.028
1093 Fitz, G., & Mann, P. (2013). Tectonic uplift mechanism of the Goodenough and Fergusson
1094 Island gneiss domes, eastern Papua New Guinea: Constraints from seismic reflection and
1095 well data. Geochemistry, Geophysics, Geosystems, 14(10), 3969-3995.
1096 https://doi.org/10.1002/ggge.20208
1097 Fletcher, J. M., Bartley, J. M., Martin, M. W., Glazner, A. F., & Walker, J. D. (1995). Large-
1098 magnitude continental extension: An example from the central Mojave metamorphic core
1099 complex. Geological Society of America Bulletin, 107(12), 1468-1483.
1100 https://doi.org/10.1130/0016-7606(1995)107%3C1468:LMCEAE%3E2.3.CO;2
1101 Floyd, J. S., Mutter, J. C., Goodliffe, A. M., & Taylor, B. (2001). Evidence for fault weakness
1102 and fluid flow within an active low-angle normal fault. Nature, 411(6839), 779.
1103 https://doi.org/10.1038/35081040
1104 Fynn, G. W., & Powell, W. J. A. (1979). The cutting and polishing of electro-optic materials.
1105 Bristol, Hilger. - 215 p.
1106 Ghosh, P., Adkins, J., Affek, H., Balta, B., Guo, W., Schauble, E. A., ... & Eiler, J. M. (2006).
1107 13C–18O bonds in carbonate minerals: a new kind of paleothermometer. Geochimica et
1108 Cosmochimica Acta, 70(6), 1439-1456. https://doi.org/10.1016/j.gca.2005.11.014
1109 Groshong Jr, R. H. (1972). Strain calculated from twinning in calcite. Geological Society of
1110 America Bulletin, 83(7), 2025-2038. https://doi.org/10.1130/0016-
1111 7606(1972)83[2025:SCFTIC]2.0.CO;2

1112 Groshong Jr, R. H. (1974). Experimental test of least-squares strain gage calculation using
1113 twinned calcite. Geological Society of America Bulletin, 85(12), 1855-1864.
1114 https://doi.org/10.1130/0016-7606(1974)85%3C1855:ETOLSG%3E2.0.CO;2
1115 Groshong Jr, R. H. (1975). Strain, fractures, and pressure solution in natural single-layer folds.
1116 Geological Society of America Bulletin, 86(10), 1363-1376.
1117 https://doi.org/10.1130/0016-7606(1975)86%3C1363:SFAPSI%3E2.0.CO;2
1118 Groshong Jr, R. H., Teufel, L. W., & Gasteiger, C. (1984). Precision and accuracy of the calcite
1119 strain-gage technique. Geological Society of America Bulletin, 95(3), 357-363.
1120 https://doi.org/10.1130/0016-7606(1984)95%3C357:PAAOTC%3E2.0.CO;2
1121 Groshong Jr, R. H. (1988). Low-temperature deformation mechanisms and their interpretation.
1122 Geological Society of America Bulletin, 100(9), 1329-1360.
1123 https://doi.org/10.1130/0016-7606(1988)100%3C1329:LTDMAT%3E2.3.CO;2
1124 Hayman, N. W., Knott, J. R., Cowan, D. S., Nemser, E., & Sarna-Wojcicki, A. M. (2003).
1125 Quaternary low-angle slip on detachment faults in Death Valley, California. Geology,
1126 31(4), 343-346. https://doi.org/10.1130/0091-
1127 7613(2003)031%3C0343:QLASOD%3E2.0.CO;2
1128 Hickman, S., & Zoback, M. (2004). Stress orientations and magnitudes in the SAFOD pilot hole.
1129 Geophysical Research Letters, 31(15). https://doi.org/10.1029/2004GL020043
1130 Hreinsdóttir, S., & Bennett, R. A. (2009). Active aseismic creep on the Alto Tiberina low-angle
1131 normal fault. Geology, 37(8), 683–686. https://doi.org/10.1130/G30194A.1
1132 Huntington, K. W., Eiler, J. M., Affek, H. P., Guo, W., Bonifacie, M., Yeung, L. Y., ... & Came,
1133 R. (2009). Methods and limitations of 'clumped'CO2 isotope (Δ47) analysis by gas-
1134 source isotope ratio mass spectrometry. Journal of Mass Spectrometry, 44(9), 1318-1329.
1135 https://doi.org/10.1002/jms.1614
1136 Ikari, M. J., Saffer, D. M., & Marone, C. (2009). Frictional and hydrologic properties of clay-rich
1137 fault gouge. Journal of Geophysical Research: Solid Earth, 114(B5).
1138 https://doi.org/10.1029/2008JB006089
1139 Jamison, W. R., & Spang, J. H. (1976). Use of calcite twin lamellae to infer differential stress.
1140 Geological Society of America Bulletin, 87(6), 868-872. https://doi.org/10.1130/0016-
1141 7606(1976)87%3C868:UOCTLT%3E2.0.CO;2

1142 Jaya, A., & Nishikawa, O. (2013). Paleostress reconstruction from calcite twin and fault–slip
1143 data using the multiple inverse method in the East Walanae fault zone: Implications for
1144 the Neogene contraction in South Sulawesi, Indonesia. Journal of Structural Geology, 55,
1145 34-49. https://doi.org/10.1016/j.jsg.2013.07.006
1146 Kanai, T., & Takagi, H. (2016). Determination of the stress conditions of the ductile-to-brittle
1147 regime along the Asuke Shear Zone, SW Japan. Journal of Structural Geology, 85, 154-
1148 167. https://doi.org/10.1016/j.jsg.2016.02.009
1149 Kilsdonk, B., & Wiltschko, D. V. (1988). Deformation mechanisms in the southeastern ramp
1150 region of the Pine Mountain block, Tennessee. Geological Society of America Bulletin,
1151 100(5), 653-664. https://doi.org/10.1130/0016-
1152 7606(1988)100%3C0653:DMITSR%3E2.3.CO;2
1153 Lacombe, O., & Laurent, P. (1996). Determination of deviatoric stress tensors based on inversion
1154 of calcite twin data from experimentally deformed monophase samples: preliminary
1155 results. Tectonophysics, 255(3-4), 189-202. https://doi.org/10.1016/0040-1951(95)00136-
1156 0
1157 Lindley, I. D. (2014). Suckling dome and the Australian–Woodlark plate boundary in eastern
1158 Papua: The geology of the Keveri and Ada'u Valleys. Australian Journal of Earth
1159 Sciences, 61(8), 1125–1147. https://doi.org/10.1080/08120099.2014.965980
1160 Lister, G. S., & Davis, G. A. (1989). The origin of metamorphic core complexes and detachment
1161 faults formed during Tertiary continental extension in the northern Colorado River
1162 region, USA. Journal of Structural Geology, 11(1), 65–94. https://doi.org/10.1016/0191-
1163 8141(89)90036-9
1164 Little, T. A., Baldwin, S. L., Fitzgerald, P. G., & Monteleone, B (2007). Continental rifting and
1165 metamorphic core complex formation ahead of the woodlark spreading ridge,
1166 D'Entrecasteaux Islands, Papua New Guinea. Tectonics, 26(1).
1167 https://doi.org/10.1029/2005TC001911
1168 Little, T. A., Hacker, B. R., Gordon, S. M., Baldwin, S. L., Fitzgerald, P. G., Ellis, S., &
1169 Korchinski, M. (2011). Diapiric exhumation of Earth's youngest (UHP) eclogites in the
1170 gneiss domes of the D'Entrecasteaux Islands, Papua New Guinea. Tectonophysics,
1171 510(1), 39-68. https://doi.org/10.1016/j.tecto.2011.06.006

1172 Little, T. A., Webber, S. M., Mizera, M., Boulton, C., Oesterle, J., Ellis, S., Boles, A., van der
1173 Pluijm, B., Norton, K., Seward, D., Biemiller, J., and Wallace, L. (2019): Evolution of a
1174 rapidly slipping, active low-angle normal fault, Suckling-Dayman Metamorphic Core
1175 Complex, SE Papua New Guinea. https://doi.org/10.1130/b35051.1
1176 Lockner, D. A., Morrow, C., Moore, D., & Hickman, S. (2011). Low strength of deep San
1177 Andreas fault gouge from SAFOD core. Nature, 472(7341), 82.
1178 https://doi.org/10.1038/nature09927
1179 Martinez, F., Goodliffe, A. M., & Taylor, B. (2001). Metamorphic core complex formation by
1180 density inversion and lower-crust extrusion. Nature, 411(6840), 930.
1181 https://doi.org/10.1038/35082042
1182 Mello, M., Bhat, H. S., Rosakis, A. J., & Kanamori, H. (2010). Identifying the unique ground
1183 motion signatures of supershear earthquakes: Theory and experiments. Tectonophysics,
1184 493(3-4), 297-326. https://doi.org/10.1016/j.tecto.2010.07.003
1185 Mizera, M. (2019). Deformational processes accommodating slip on an active low-angle normal
1186 fault, Suckling-Dayman Metamorphic Core Complex, Papua New Guinea, (Doctoral
1187 dissertation). Wellington, New Zealand: Victoria University of Wellington. Retrieved
1188 from http://hdl.handle.net/10063/8666
1189 Mizera, M., Little, T. A., Biemiller, J., Ellis, S., Webber, S., & Norton, K. P. (2019). Structural
1190 and geomorphic evidence for rolling-hinge style deformation of an active continental
1191 low-angle normal fault, SE Papua New Guinea. Tectonics, 38(5), 1556–1583.
1192 https://doi.org/10.1029/2018TC005167
1193 Mizera, M., Little, T., Prior, D. J. & Smith, E. G. C. (2021). Strength and Stress Evolution of the
1194 Active Mai'iu Low-Angle Normal Fault, Data Repository. Mendeley Data, V1.
1195 http://dx.doi.org/10.17632/mkpgbs4hf3.1
1196 Mizera, M., Little, T., Boulton, C., Prior, D., Watson, E., Biemiller, J., ... & Shigematsu, N.
1197 (2020). Slow-to-Fast Deformation in Mafic Fault Rocks on an Active Low-Angle Normal
1198 Fault, Woodlark Rift, SE Papua New Guinea. Geochemistry, Geophysics, Geosystems,
1199 e2020GC009171. https://doi.org/10.1029/2020GC009171
1200 Morrow, C. A., Moore, D. E., & Lockner, D. A. (2017). Frictional strength of wet and dry
1201 montmorillonite. Journal of Geophysical Research: Solid Earth, 122(5), 3392-3409.
1202 https://doi.org/10.1002/2016JB013658

Österle, J. (2019). The thermo-tectonic evolution of the Suckling-Dayman metamorphic core complex, southeastern Papua New Guinea (Doctoral dissertation, Victoria University of Wellington). https://hdl.handle.net/10063/8241

Österle, J. E., Little, T. A., Seward, D., Stockli, D. F., & Gamble, J. (2020). The petrology, geochronology and tectono-magmatic setting of igneous rocks in the Suckling-Dayman metamorphic core complex, Papua New Guinea. Gondwana Research, 83, 390–414. https://doi.org/10.1016/j.gr.2020.01.014

Otsubo, M., & Yamaji, A. (2006). Improved resolution of the multiple inverse method by eliminating erroneous solutions. Computers & geosciences, 32(8), 1221-1227. https://doi.org/10.1016/j.cageo.2005.10.022

Otsubo, M., Yamaji, A., & Kubo, A. (2008). Determination of stresses from heterogeneous focal mechanism data: An adaptation of the multiple inverse method. Tectonophysics, 457(3-4), 150-160. https://doi.org/10.1016/j.tecto.2008.06.012

Passey, B. H., Levin, N. E., Cerling, T. E., Brown, F. H., & Eiler, J. M. (2010). High-temperature environments of human evolution in East Africa based on bond ordering in paleosol carbonates. Proceedings of the National Academy of Sciences, 107(25), 11245-11249. https://doi.org/10.1073/pnas.1001824107

Passey, B. H., & Henkes, G. A. (2012). Carbonate clumped isotope bond reordering and geospeedometry. Earth and Planetary Science Letters, 351, 223-236. https://doi.org/10.1016/j.epsl.2012.07.021

Platt, J. P., Behr, W. M., & Cooper, F. J. (2015). Metamorphic core complexes: Windows into the mechanics and rheology of the crust. Journal of the Geological Society, 172(1), 9–27. https://doi.org/10.1144/jgs2014-036

Platt, J. P., & De Bresser, J. H. P. (2017). Stress dependence of microstructures in experimentally deformed calcite. Journal of Structural Geology, 105, 80-87. https://doi.org/10.1016/j.jsg.2017.10.012

Reston, T. (2020). On the rotation and frictional lock-up of normal faults: Explaining the dip distribution of normal fault earthquakes and resolving the low-angle normal fault paradox. Tectonophysics, 790, 228550. https://doi.org/10.1016/j.tecto.2020.228550

Rigo, A., Lyon-Caen, H., Armijo, R., Deschamps, A., Hatzfeld, D., Makropoulos, K., & Kassaras, I. (1996). A microseismic study in the western part of the Gulf of Corinth

(Greece): Implications for large-scale normal faulting mechanisms. Geophysical Journal International, 126(3), 663–688. https://doi.org/10.1111/j.1365-246X.1996.tb04697.x

Rowe, K. J., & Rutter, E. H. (1990). Palaeostress estimation using calcite twinning: experimental calibration and application to nature. Journal of Structural Geology, 12(1), 1-17. https://doi.org/10.1016/0191-8141(90)90044-Y

Rutter, E. H., Faulkner, D. R., Brodie, K. H., Phillips, R. J., & Searle, M. P. (2007). Rock deformation processes in the Karakoram fault zone, Eastern Karakoram, Ladakh, NW India. Journal of Structural Geology, 29(8), 1315-1326. https://doi.org/10.1016/j.jsg.2007.05.001

Ryb, U., Lloyd, M. K., Stolper, D. A., & Eiler, J. M. (2017). The clumped-isotope geochemistry of exhumed marbles from Naxos, Greece. Earth and Planetary Science Letters, 470, 1-12. https://doi.org/10.1016/j.epsl.2017.04.026

Rybacki, E., Evans, B., Janssen, C., Wirth, R., & Dresen, G. (2013). Influence of stress, temperature, and strain on calcite twins constrained by deformation experiments. Tectonophysics, 601, 20-36. https://doi.org/10.1016/j.tecto.2013.04.021

Schultz, R. A. (1993). Brittle strength of basaltic rock masses with applications to Venus. Journal of Geophysical Research: Planets, 98(E6), 10883-10895. https://doi.org/10.1029/93JE00691

Sibson, R. H. (1985). A note on fault reactivation. Journal of Structural Geology, 7(6), 751–754. https://doi.org/10.1016/0191-8141(85)90150-6

Singleton, J. S. (2013). Development of extension-parallel corrugations in the Buckskin-Rawhide metamorphic core complex, west-central Arizona. Bulletin, 125(3-4), 453-472. https://doi.org/10.1130/B30672.1

Smith, I. E., & Davies, H. L. (1976). Geology of the southeast Papuan mainland. Bureau of mineral resources, geology and geophysics. Canberra, ACT: Australian Publishing Service.

Speckbacher, R., Behrmann, J. H., Nagel, T. J., Stipp, M., & Mahlke, J. (2012). Fluid flow and metasomatic fault weakening in the Moresby Seamount detachment, Woodlark Basin, offshore Papua New Guinea. Geochemistry, Geophysics, Geosystems, 13(11). https://doi.org/10.1029/2012GC004407

1264 Speckbacher, R., Stipp, M., Behrmann, J. H., & Heidelbach, F. (2013). Fluid-assisted fracturing,
1265 cataclasis, and resulting plastic flow in mylonites from the Moresby Seamount
1266 detachment, Woodlark Basin. Journal of Structural Geology, 56, 156–171.
1267 https://doi.org/10.1016/j.jsg.2013.10.001
1268 Spencer, J. E. (2010). Structural analysis of three extensional detachment faults with data from
1269 the 2000 Space-Shuttle Radar Topography Mission. Geological Society of America
1270 Today, 20(8), 4–10. https://doi.org/10.1130/GSATG59A.1
1271 Stolper, D. A., & Eiler, J. M. (2015). The kinetics of solid-state isotope-exchange reactions for
1272 clumped isotopes: A study of inorganic calcites and apatites from natural and
1273 experimental samples. American Journal of Science, 315(5), 363-411.
1274 https://doi.org/10.2475/05.2015.01
1275 Taylor, B., & Huchon, P. (2002). Active continental extension in the western Woodlark Basin: A
1276 synthesis of Leg 180 results. In P. Huchon, B. Taylor, & A. Klaus (Eds.), Proc. ODP, Sci.
1277 Results (Vol. 180, pp. 1–36). College Station, TX: Ocean Drilling Program.
1278 https://doi.org/10.2973/odp.proc.sr.180.150.2002
1279 Tjhin, K. T. (1976). Trobriand Basin exploration, Papua New Guinea. The APPEA Journal,
1280 16(1), 81-90. https://doi.org/10.1071/AJ75008
1281 Tregoning, P., Lambeck, K., Stolz, A., Morgan, P., McClusky, S. C., Beek, P., & Murphy, B.
1282 (1998). Estimation of current plate motions in Papua New Guinea from global
1283 positioning system observations. Journal of Geophysical Research, 103(B6), 12181–
1284 12203. https://doi.org/10.1029/97JB03676
1285 Tullis, T. E. (1980). The use of mechanical twinning in minerals as a measure of shear stress
1286 magnitudes. Journal of Geophysical Research: Solid Earth, 85(B11), 6263-6268.
1287 https://doi.org/10.1029/JB085iB11p06263
1288 Turner, F. J. (1953). Nature and dynamic interpretation of deformation lamellae in calcite of
1289 three marbles. American Journal of Science, 251(4), 276-298.
1290 https://doi.org/10.2475/ajs.251.4.276
1291 Turner, F. J. (1962, January). Compression and tension axes deduced from (0112) Twinning in
1292 Calcite. In Journal of Geophysical Research (Vol. 67, No. 4, p. 1660). 2000 FLORIDA
1293 AVE NW, WASHINGTON, DC 20009: AMER GEOPHYSICAL UNION.

1294 Valcke, S. L. A., De Bresser, J. H. P., Pennock, G. M., & Drury, M. R. (2015). Influence of
1295 deformation conditions on the development of heterogeneous recrystallization
1296 microstructures in experimentally deformed Carrara marble. Geological Society, London,
1297 Special Publications, 409(1), 175-200. https://doi.org/10.1144/SP409.4
1298 Wallace, L. M., Stevens, C., Silver, E., McCaffrey, R., Loratung, W., Hasiata, S., & Taugaloidi,
1299 J. (2004). GPS and seismological constraints on active tectonics and arc-continent
1300 collision in Papua New Guinea: Implications for mechanics of microplate rotations in a
1301 plate boundary zone. Journal of Geophysical Research, 109(B5).
1302 https://doi.org/10.1029/2003JB002481
1303 Wallace, L. M., Ellis, S., Little, T., Tregoning, P., Palmer, N., Rosa, R., & Kwazi, J. (2014).
1304 Continental breakup and UHP rock exhumation in action: GPS results from the Woodlark
1305 Rift, Papua New Guinea. Geochemistry, Geophysics. Geosystems, 15(11), 4267–4290.
1306 https://doi.org/10.1002/2014GC005458
1307 Watson, E. J., Turner, G. M., Little, T. A., & Piispa, E. J. (2021). Using paleomagnetism to test
1308 rolling hinge behaviour of an active continental low angle normal fault, Papua New
1309 Guinea. Earth and Planetary Science Letters, 558, 116745.
1310 Webb, L. E., Baldwin, S. L., Little, T. A., & Fitzgerald, P. G. (2008). Can microplate rotation
1311 drive subduction inversion?. Geology, 36(10), 823–826.
1312 https://doi.org/10.1130/G25134A.1
1313 Webber, S., Norton, K. P., Little, T. A., Wallace, L. M., & Ellis, S. (2018). How fast can low-
1314 angle normal faults slip? Insights from cosmogenic exposure dating of the active Mai'iu
1315 fault, Papua New Guinea. Geology, 46(3), 227–230. https://doi.org/10.1130/G39736.1
1316 Webber, S., Little, T. A., Norton, K. P., Österle, J., Mizera, M., Seward, D., & Holden, G.
1317 (2020). Progressive back-warping of a rider block atop an actively exhuming, continental
1318 low-angle normal fault. Journal of Structural Geology, 130, 103906.
1319 https://doi.org/10.1016/j.jsg.2019.103906
1320 Weber, J. C., Ferrill, D. A., & Roden-Tice, M. K. (2001). Calcite and quartz microstructural
1321 geothermometry of low-grade metasedimentary rocks, Northern Range, Trinidad. Journal
1322 of Structural Geology, 23(1), 93-112. https://doi.org/10.1016/S0191-8141(00)00066-3

Westaway, R. (2005). Active low-angle normal faulting in the Woodlark extensional province, Papua New Guinea: A physical model. Tectonics, 24(6). https://doi.org/10.1029/2004TC001744

Whitney, D. L., Teyssier, C., Rey, P., & Buck, W. R. (2013). Continental and oceanic core complexes. The Geological Society of America Bulletin, 125(3–4), 273–298. https://doi.org/10.1130/B30754.1

Yamaji, A. (2000). The multiple inverse method: a new technique to separate stresses from heterogeneous fault-slip data. Journal of Structural Geology, 22(4), 441-452. https://doi.org/10.1016/S0191-8141(99)00163-7

Yamaji, A., & Sato, K. (2006). Distances for the solutions of stress tensor inversion in relation to misfit angles that accompany the solutions. Geophysical Journal International, 167(2), 933-942. https://doi.org/10.1111/j.1365-246X.2006.03188.x

Yamaji, A. (2015). How tightly does calcite e-twin constrain stress?. Journal of Structural Geology, 72, 83-95. https://doi.org/10.1016/j.jsg.2015.01.008

Yin, A. (1989). Origin of regional, rooted low-angle normal faults: A mechanical model and its tectonic implications. Tectonics, 8(3), 469–482. https://doi.org/10.1029/TC008i003p00469

Zoback, M. D., & Harjes, H. P. (1997). Injection-induced earthquakes and crustal stress at 9 km depth at the KTB deep drilling site, Germany. Journal of Geophysical Research: Solid Earth, 102(B8), 18477-18491. https://doi.org/10.1029/96JB02814

References from the Supporting Information

Angelier, J. (1979). Determination of the mean principal directions of stresses for a given fault population. Tectonophysics, 56(3-4), T17-T26. https://doi.org/10.1016/0040-1951(79)90081-7

Barnhoorn, A., Bystricky, M., Burlini, L., & Kunze, K. (2004). The role of recrystallisation on the deformation behaviour of calcite rocks: large strain torsion experiments on Carrara marble. Journal of Structural Geology, 26(5), 885-903. https://doi.org/10.1016/j.jsg.2003.11.024

1351 Caffi , P. (2008). Evolution of an Active Metamorphic Core Complex, Suckling-Dayman Massif,
1352 Eastern Papua New Guinea [B.Sc. (Honor's) thesis]: Sydney, Australia: Macquarie
1353 University, 113 p.
1354 De Bresser, J. H. P., Evans, B., & Renner, J. (2002). On estimating the strength of calcite rocks
1355 under natural conditions. Geological Society, London, Special Publications, 200(1), 309-
1356 329. https://doi.org/10.1144/GSL.SP.2001.200.01.18
1357 De Bresser, J. H. P., Urai, J. L., & Olgaard, D. L. (2005). Effect of water on the strength and
1358 microstructure of Carrara marble axially compressed at high temperature. Journal of
1359 Structural Geology, 27(2), 265-281. https://doi.org/10.1016/j.jsg.2004.10.002
1360 Ebert, A., Herwegh, M., Ramseyer, K., & Decrouez, D. (2008). Calcite microstructures as paleo-
1361 thermometer and indicator of shear zone width. Geotectonic research, 95(38), 36-38.
1362 https://doi.org/10.1127/1864-5658/08/9501-0036
1363 Etchecopar, A., Vasseur, G., & Daignieres, M. (1981). An inverse problem in microtectonics for
1364 the determination of stress tensors from fault striation analysis. Journal of Structural
1365 Geology, 3(1), 51-65. https://doi.org/10.1016/0191-8141(81)90056-0
1366 Ferrill, D. A. (1991). Calcite twin widths and intensities as metamorphic indicators in natural
1367 low-temperature deformation of limestone. Journal of Structural Geology, 13(6), 667-
1368 675. https://doi.org/10.1016/0191-8141(91)90029-I
1369 Karaman, K., Cihangir, F., & Kesimal, A. (2013). Kaya Malzemesinin Kohezyon ve İçsel
1370 Sürtünme Açısının Dolaylı Yöntemlerle İrdelenmesi. Mehmet Akif Ersoy Üniversitesi
1371 Fen Bilimleri Enstitüsü Dergisi, 4(2), 13-19. Retrieved from
1372 https://dergipark.org.tr/en/pub/makufebed/issue/19420/206536
1373 Ketcham, R. A. (1996). Thermal models of core-complex evolution in Arizona and New Guinea:
1374 Implications for ancient cooling paths and present-day heat flow. Tectonics, 15(5), 933-
1375 951. https://doi.org/10.1029/96TC00033
1376 Labuz J.F., Zang A. (2012). Mohr–Coulomb Failure Criterion. In: Ulusay R. (eds) The ISRM
1377 Suggested Methods for Rock Characterization, Testing and Monitoring: 2007-2014.
1378 Springer, Cham. https://doi.org/10.1007/978-3-319-07713-0_19
1379 O'Neil, J. R., & Taylor Jr, H. P. (1969). Oxygen isotope equilibrium between muscovite and
1380 water. Journal of Geophysical Research, 74(25), 6012-6022.
1381 https://doi.org/10.1029/JB074i025p06012

1382 Renner, J., Evans, B., & Siddiqi, G. (2002). Dislocation creep of calcite. Journal of Geophysical
1383 Research: Solid Earth, 107(B12). https://doi.org/10.1029/2001JB001680
1384 Rutter, E. H. (1995). Experimental study of the influence of stress, temperature, and strain on the
1385 dynamic recrystallization of Carrara marble. Journal of Geophysical Research: Solid
1386 Earth, 100(B12), 24651-24663. https://doi.org/10.1029/95JB02500
1387 Rybacki, E., Janssen, C., Wirth, R., Chen, K., Wenk, H. R., Stromeyer, D., & Dresen, G. (2011).
1388 Low-temperature deformation in calcite veins of SAFOD core samples (San Andreas
1389 Fault)—microstructural analysis and implications for fault rheology. Tectonophysics,
1390 509(1-2), 107-119. https://doi.org/10.1016/j.tecto.2011.05.014
1391 Schmid, S. M., Paterson, M. S., & Boland, J. N. (1980). High temperature flow and dynamic
1392 recrystallization in Carrara marble. Tectonophysics, 65(3-4), 245-280.
1393 https://doi.org/10.1016/0040-1951(80)90077-3
1394 Sibson, R. H. (1998). Brittle failure mode plots for compressional and extensional tectonic
1395 regimes. Journal of Structural Geology, 20(5), 655-660. https://doi.org/10.1016/S0191-
1396 8141(98)00116-3
1397 Ter Heege, J. H., De Bresser, J. H. P., & Spiers, C. J. (2002). The influence of dynamic
1398 recrystallization on the grain size distribution and rheological behaviour of Carrara
1399 marble deformed in axial compression. Geological Society, London, Special
1400 Publications, 200(1), 331-353. https://doi.org/10.1144/GSL.SP.2001.200.01.19
1401 Tielke, J. A. (2010). Development and application of a method for determining paleostress from
1402 calcite deformation twins using electron backscatter diffraction: M.s. thesis, South
1403 Dakota School of Mines and Technology, 133 p.
1404 Walker, A. N., Rutter, E. H., & Brodie, K. H. (1990). Experimental study of grain-size sensitive
1405 flow of synthetic, hot-pressed calcite rocks. Geological Society, London, Special
1406 Publications, 54(1), 259-284. https://doi.org/10.1144/GSL.SP.1990.054.01.24